1. AGENCY USE ONLY (Leave blank)	2. REPORT DATE 19 November 1994	3. REPORT TYPE AND DATES COVERED Final Technical, 7/1/92 - 10/31/94	
4. TITLE AND SUBTITLE Modeling Liquid Jet Atomization Processes		**5. FUNDING NUMBERS** F49620-92-J-0390	
6. AUTHOR(S) Stephen D. Heister			
7. PERFORMING ORGANIZATION NAME(S) AND ADDRESS(ES) School of Aeronautics & Astronautics Purdue University 1282 Grissom Hall West Lafayette, IN 47907-1282		**8. PERFORMING ORGANIZATION REPORT NUMBER** AFOSR-TR· 9 5 - 0 3 9 7	
9. SPONSORING/MONITORING AGENCY NAME(S) AND ADDRESS(ES) AFOSR/NA Dr. Birkan 110 Duncan Avenue, Suite B115 Bolling AFB, DC 20332-0001	NA	**10. SPONSORING/MONITORING AGENCY REPORT NUMBER**	

11. SUPPLEMENTARY NOTES

DTIC SELECTED JUN 1 4 1995 F

12a. DISTRIBUTION/AVAILABILITY STATEMENT Approved for public release; distribution is unlimited	12b. DISTRIBUTION CODE

19950612 105

13. ABSTRACT (Maximum 200 words)

This report summarizes efforts in developing an analytic/numerical modeling capability for both steady and unsteady liquid jet atmization processes. The research involves the application of boundary element methods to model nonlinear deformation of liquid surfaces. An inviscid model has been developed to investigate dynamics of a finite-length jet which includes the presence of the orifice flow passages. In addition, a second model has been developed to simulate gas-phase interactions with the distorting jet surface. Preliminary developments associated with a viscous model are also discussed.

DTIC QUALITY INSPECTED 3

14. SUBJECT TERMS atomization, free surfaces, liquid rocket injectors, boundary element methods			15. NUMBER OF PAGES 63
			16. PRICE CODE
17. SECURITY CLASSIFICATION OF REPORT Unclassified	18. SECURITY CLASSIFICATION OF THIS PAGE Unclassified	19. SECURITY CLASSIFICATION OF ABSTRACT Unclassified	20. LIMITATION OF ABSTRACT UL

AFOSR Contract F49620-92-J-0390

MODELING LIQUID JET ATOMIZATION PROCESSES

Stephen D. Heister, Associate Professor
School of Aeronautics and Astronautics
Purdue University
1282 Grissom Hall
West Lafayette, IN 47907-1282

Accesion For		
NTIS CRA&I	☑	
DTIC TAB	☐	
Unannounced	☐	
Justification		
By		
Distribution /		
Availability Codes		
Dist	Avail and / or Special	
A-1		

19 November 1994

Final Technical Report for Period 1 July 1992 - 31 October 1994

Approved for Public Release,
Distribution is Unlimited

Summary

The atomization of liquid jets is a fundamental problem of particular interest in determining the performance and combustion stability of liquid rocket engines. This research effort is focused on a new analytic treatment of this free surface flow utilizing Boundary Element Methods (BEMs). This analytic approach is attractive for problems of this nature due to its inherent efficiency (as compared to more traditional CFD methods) and its high accuracy in determining the time-dependent evolution of the free surface for a reasonable computational expense.

Ultimately, the goal of this project is aimed at developing a complete simulation of an atomization process. Toward this end, we have completed an axisymmetric, inviscid simulation. This step was necessary in allowing us to develop a general surface tracking capability. In connection with this approach, a new capability has been developed to model gas/liquid flows with a free surface utilizing the BEM approach. In addition, a new technique has been developed to model an atomization process well beyond the initial droplet shedding event for an arbitrary orifice geometry and injection conditions.

1   Research Objectives

The understanding of the complex combustion phenomena present in liquid rocket engines begins with the fundamental process of fuel and oxidizer jet atomization. Since the atomization process can be greatly effected by acoustic disturbances[1], it appears as a primary focus[2] in studies involving combustion stability. For this reason, both analytic and experimental research are necessary to increase our understanding of the complex interactions between the droplet field formed by the jet and the combustion process.

The analytic/numerical techniques described in this report center on the use of Boundary Element Methods (BEMs) which can be used to accurately describe the time-dependent evolution of waves forming on the surfaces of the jet. The BEM approach is superior to more traditional Computational Fluid Dynamic (CFD) methods since the BEM formulation requires a discretization of only the external surface of the jet rather than the entire liquid domain. This distinction is important for the highly-distorted surface shapes (and hence highly-distorted CFD grids) required to properly model these processes. In addition, a complex regridding would be required of a traditional CFD implementation as droplets are shed from the periphery of the jet. Models developed under this research grant have successfully demonstrated this capability utilizing the BEM approach.

With these ideas in mind, this research effort seeks to develop a general BEM capable of modeling the atomization process for an arbitrary fluid under arbitrary injection conditions and orifice geometry. This capability would be utilized to predict the primary atomization event and permit interface to secondary atomization and collision/coalescence models further characterizing the spray. The following section discusses the technical status of the research. Section 3 describes professional activies, while Section 4 gives the references for this report.

2   Status of the Research

Due to the unusual starting time for the contract (1 July, 1992), graduate student participation in this research effort was delayed for five months. As a result of this situation, a four month contract extension was requested (and granted) as indicated in the letters shown in Appendix A. This development led to a new schedule for the grant reporting requirements (see Appendix A) which changed the Final Report Due Date from 31 August, 1994 to 31 December, 1994. This

document therefore serves to report on the entire 28 month grant period dating from 1 July, 1992 to 31 October, 1994.

During this timeframe, two inviscid computer codes have been developed and the development of a viscous code is about 50% complete.

The first of the inviscid codes demonstrated a capability of modeling an atomization process for an orifice of arbitrary geometry through a large number of droplet pinchoff events. The model represents the first numerical approach which includes the impact of orifice geometry (i.e. finite jet length) on the atomization process within the flow regimes of interest. This model is described in Section 2.1 of this report. The second inviscid model represents the genesis of a new BEM capability for general gas/liquid flows involving a free surface. The model has been utilized to characterize atomization of a liquid jet in the wind-induced atomization regime. This model is described in Section 2.2 of this document. Development of a viscous capability are summarized in Section 2.3, while future efforts to be applied to this research area are discussed in Section 2.4.

2.1 BEM for a Finite-Length Liquid Jet

Historically, most analytic or numerical liquid jet simulations[3-10] have ignored the presence of the orifice and its contribution to the atomization process. This assumption is quite valid in the event that the breakup of the jet is far downstream of the injection point. However, in the atomization regime of interest to liquid rocket engine injectors, jet breakup occurs in the immediate proximity of the orifice. For this reason, it is necessary to include the presence of the orifice (and its specific design geometry) in any simulation within this regime.

In addition, to develop a complete model of the spray formation process, it is also necessary to run a simulation through numerous droplet pinchoff events. While this capability has been demonstrated by researchers utilizing BEMs, it has generally been included to address the dynamics of a single droplet shed from a column of fluid[9,10]. Here, a more general capability is desired such that the dynamics of the main body of fluid can be addressed after the pinchoff event. Appendix B contains a manuscript recently submitted to *Atomization and Sprays* which describes the elements of the model created for simulation of a finite-length liquid jet. Additional details can be found in Refs. 11 and 12. A brief summary of the elements of this model is provided below.

Figure 1 (also see Appendix B, Fig. 5) shows the computational domain utilized for a typical simulation. A hybrid grid is employed which enables nodes within the orifice passage to remain fixed, while nodes on the free surface are tracked in a Lagrangian sense with the local fluid velocity. Axisymmetric, inviscid flow is assumed within the liquid, and pressure variations in the gas (due to the presence of the liquid) are neglected. These simplifying assumptions permit us to focus on the development of a scheme for tracking the complex evolution of a free surface during atomization processes. A precise definition of the free surface is required for flows of this nature in which surface tension (and hence surface curvature) plays a substantial role.

The major features incorporated into this model include:

- Laplace Solver - This module uses the BEM formulation to solve the differential equation (Laplace's equation) in the liquid domain. If ϕ represents the velocity potential in the liquid, we are focusing on the solution of $\nabla^2 \phi = 0$ in this module.

- Time Integration - A high accuracy, fourth-order time integration scheme (using the Runge-Kutta method) is employed to insure precise movement of the surface nodes. The Bernoulli and kinematic boundary conditions specify the time-dependent behavior of the velocity potential and surface velocity. These equations are integrated using the Runge-Kutta approach. The time step for the integration procedure is set dynamically during the integration in order to insure that nodes move only a small fraction of the local nodal spacing on a given time step.
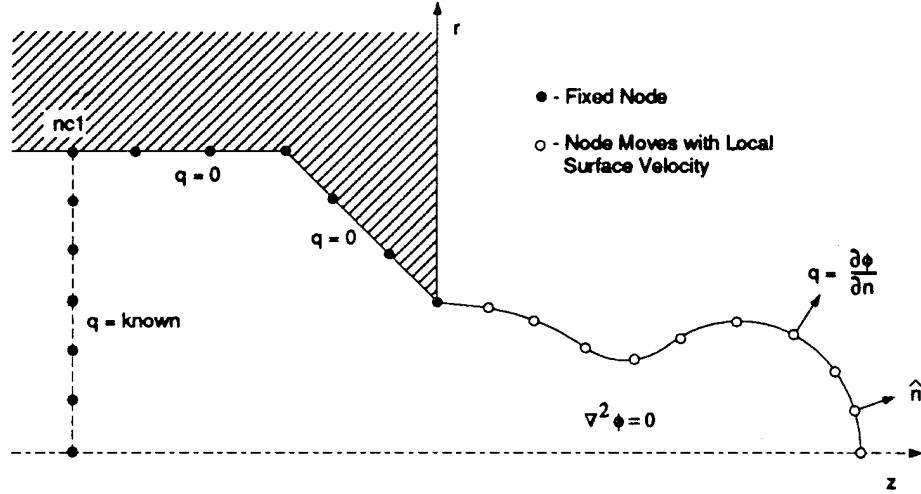
2

Figure 1: Finite-Length Liquid Jet Computational Domain.

- Free Surface Module - Fourth-order centered differencing is used to accurately define surface curvature at all times. Surface slope is obtained using the method of Medina, et. al.[13].

- Surface Regridding Module - To avoid "bunching" of points in high curvature regions, nodes are redistributed at equal length intervals along the surface at each time step. This regridding procedure is implemented by fitting the surface coordinates (and the velocity potential) with cubic splines. Points are then redistributed at equal length intervals by interpolating values from cubic spline curvefits. In addition, this module includes the capability to dynamically change the number of nodes along the surface. Nodes can be added near the orifice as more fluid issues from the nozzle. In addition, nodes can be removed from the simulation when droplet pinchoff occurs.

The Time Integration, Free Surface, and Surface Regridding Modules are developments which will be common to future BEM codes which will include viscous effects. For this reason, it is obvious that the development of an inviscid model provides great insight and capability to tackle the more difficult viscous problem. Numerous results of simulations performed with the model are included in Appendix B. Of particular interest is the simulation of a dripping faucet. This simulation is quite appropriate in that atomization occurs in close proximity to the orifice, thus providing a means to validate this aspect of the model.

The geometry shown in Fig. 1 was used to simulate the experiments of Wu and Schelly[14]. These experiments revealed both chaotic and bimodal droplet size formation within the dripping flow regime. These authors attempted to correlate this behavior with chaos theory. Results of our simulation are shown in Fig. 2 below. The results indicate that both chaotic and bimodal droplet size formation is predicted using the deterministic model. In analyzing results, we found that this behavior is attributed to interactions of disturbances (caused by the pinchoff event) with the orifice. Therefore, the simulation lends confidence to a similar treatment which will be applied to a viscous simulation in the coming year.

2.2 Atomization Processes in the Wind-Induced Regime

Atomization processes inside liquid rocket engines can be greatly effected by the influence of high density combustion gases influencing the pressure distribution on liquid ligaments formed during
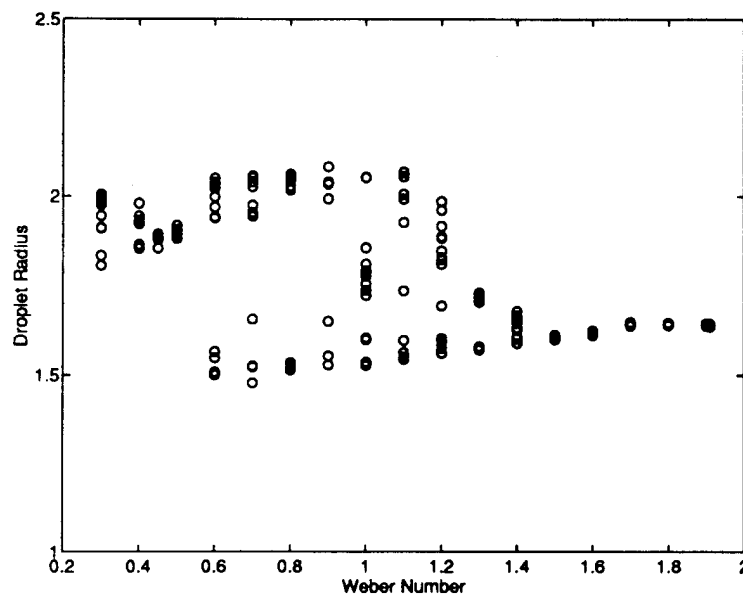
Figure 2: Droplet Size for Dripping Flow, Bo=0.204.

early stages of atomization. To address the effects of atomization in this "wind-induced" regime, a BEM simulation was developed[15-17] in accordance with the developments described above. A detailed description of the model and results of simulations is attached in Appendix C. Brief highlights of the results will be discussed below.

For this calculation, an infinite jet with a very small perturbation is assumed for modeling purposes. In accordance with these assumptions, the computational domain is shown in Fig. 3 (adopted from Fig. 2 in Appendix C). The boundary element formulation is utilized to solve for both liquid and gas flowfields. The major development required for a model of this type is a stable, accurate treatment of the coupled set of nonlinear boundary conditions present at the gas/liquid interface. In Appendix C, the new treatment developed for this application is described in detail. Results indicate that the methodology employed is quite general, and can easily be applied to a variety of other gas/liquid flow problems.

The model has been shown to reproduce both linear and nonlinear results of previous researchers. Moreover, the model predicts the presence (and size) of satellite droplets formed within the first wind-induced regime. Figure 4 depicts a comparison of predicted droplet sizes with measurements of researchers indicating a good predictive capability. The model has also been utilized to predict the transition between first and second wind-induced regimes. This transition, which can only be evaluated with a nonlinear model, corresponds to the point where droplets are shed at the jet periphery, rather than at the centerline of the jet. Figure 5 presents results of a simulation near this transition point. Results indicate that the transition occurs at a gas-based Weber number of approximately 2.5.

In addition, the code has been utilized to model the development of ripples on the surface of a high-speed liquid jet operating in the second wind-induced regime. Here we should note that this regime is consistent with injection conditions in some liquid rocket engine injectors. A simulation of the process is shown in Figure 6. The inviscid gas-phase formulation employed leads to a "spiked" appearance. Inclusion of gas-phase viscosity is required to improve the simulation at large distortions (where boundary layer separation are presumed to occur). Nevertheless, this model represents the first nonlinear simulation of gas/liquid flows within this high speed flow regime.
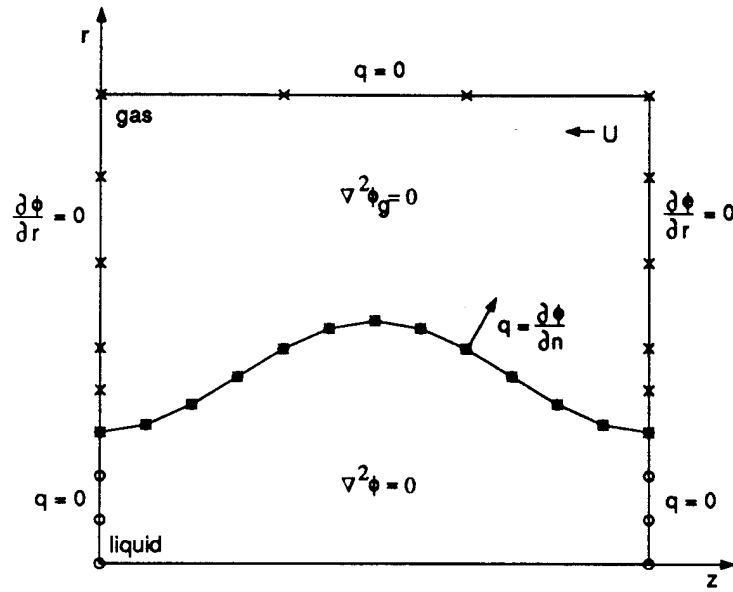
4

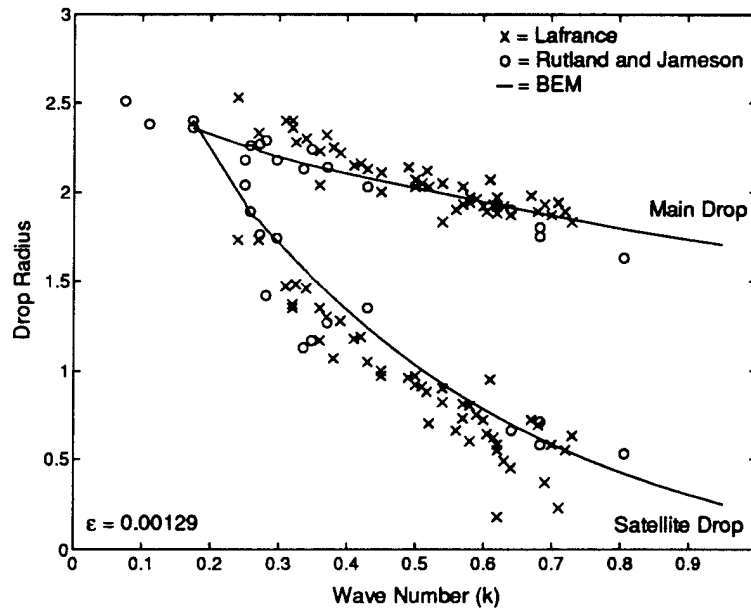Figure 3: Schematic of Computational Domain Denoting Boundary Conditions

Figure 4: Comparison of the BEM to the Drop Sizes of Rutland and Jameson[8] (o) and Lafrance[7] (x) for Main and Satellite Drops, $\epsilon = 0.00129$
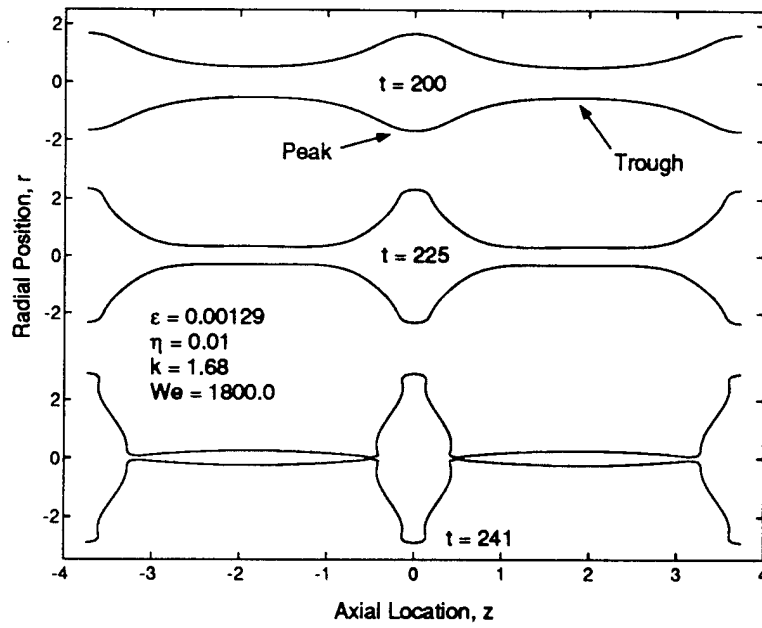
5

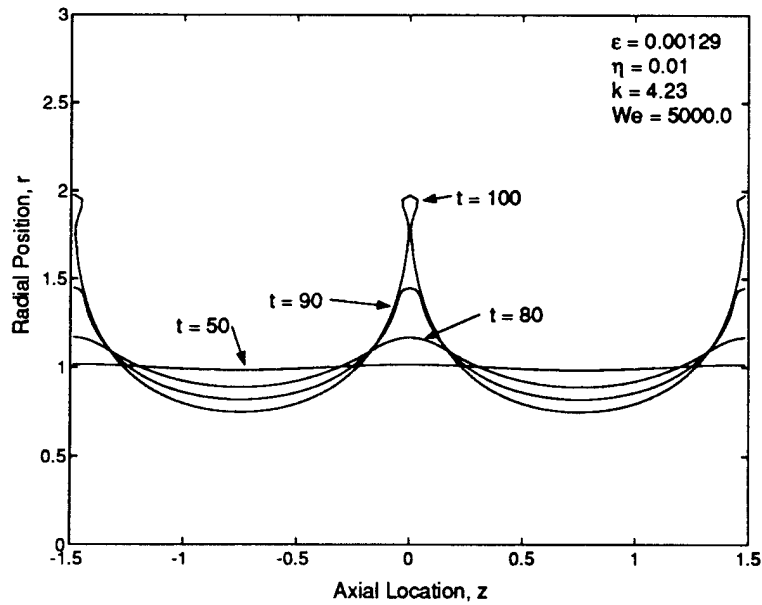Figure 5: Nonlinear Jet Evolution in the Transition Region

Figure 6: Nonlinear Jet Evolution in the Second Wind-Induced Regime

6

2.3 Current Status of Viscous Code Development

Since this research project has been granted a continuation (AFOSR Contract F49620-94-1-0151), it is appropriate to discuss the future directions of this work within the context of this final report. As noted in the previous discussion, the ultimate goal of this work is to establish a simulation of the viscous atomization process. To this end, we began the work based on the simpler inviscid formulation in order to gain experience in boundary element techniques and to validate free surface modules required for viscous simulations.

Prior to the development of a viscous BEM capability, an extensive literature review was conducted. While several authors have developed viscous simulations using BEM techniques, many of these methods use alternate approaches in viscous zones[18,19], or are restricted to Stokes flow regimes at very low Reynolds numbers[20-22]. Recent developments[23-25] indicate that a full viscous BEM solution is now at hand. In particular, the methodology developed by Jin and Brown[25], is very attractive for free surface problems in that it employs a Lagrangian point of view which is natural to use for tracking a free surface.

Jin and Brown described a method for treating the Lagrangian time derivative using the *traction-velocity* boundary element formulation. This formulation has been applied successfully to steady free surface flows by various researchers[26,27]. It is important to note that Jin and Brown's technique for unsteady problems has never been implemented in an actual code.

For the unsteady problem, Jin and Brown propose a treatment utilizing the *Dual Reciprocity Method*, (DRM) to aid in mapping domain integrals (which appear due to presence of unsteady terms) to the boundary. The DRM represents a new technique developed within the past decade by the BEM research group[23] at Wessex Institute of Technology in Southampton, United Kingdom. Dr. Carlos Brebbia, the world's leading authority on BEM development, heads this research group. It is only within the past two years that a book on DRM implementation has become available. effectively maps domain integrals to the boundary by utilizing shape functions which are forms of the governing equations themselves. Only a few interior nodes must be utilized in such a formulation; an attractive feature for boundary-based solution techniques.

To develop a free surface code utilizing the methodology described above is quite daunting since a full unsteady capability using the DRM is required. For this reason, an incremental approach was adopted whereby a series of models with increasing complexity are developed. While the ultimate goal is to create an axisymmetric, viscous, unsteady code, the following approach has been adopted:

1. Develop a steady, two-dimensional viscous code. Validate this model by performing a simulation of general Couette flow (flow in a channel) using various computational domains. This code provides insight into the traction-velocity formulation and the required treatment of singularities and multi-valued tractions at domain corners.

2. Test case simulation using the DRM on a problem with a known analytic solution[28]. This validation aids in gaining experience in applying the DRM to complex differential equations.

3. Extend the two-dimensional steady model to handle unsteady problems via implementation of the DRM on the system of viscous equations. Validate this code by performing a simulation of Stokes's first problem (impulsively-started infinite flat plate). This development will permit the determination of the number of internal nodes required for accuracy with the DRM.

4. Apply the Lagrangian treatment of boundary nodes per Jin and Brown to the two-dimensional, unsteady code. The addition of a free surface module at this point will give the capability to investigate the stability of liquid sheets.

7

5. Development of an axisymmetric model using the methodology created for the two-dimensional code. A steady model will verify the new integrations in the traction-velocity formulation, a second model will verify the axisymmetric formulation of the DRM, followed by a full unsteady model in Lagrangian form.

At the present time, Tasks #1 and 2 have been completed, and Task #3 is well underway. The two-dimensional formulation was implemented first due to the relative simplicity of the fundamental solutions (Green's functions) for this case. For the axisymmetric case, the Green's functions are much more complex. Items #4 and 5 will be accomplished under a follow-on contract which will be concluded in June, 1996.

2.4   Future Efforts - Viscous Flows

Upon completion of the tasks outlined in the previous list, we shall have the capability of modeling both two-dimensional and axisymmetric flows with free surfaces. These new models will aid in enhancing the understanding of complex, nonlinear atomization processes germaine to both rocket and airbreathing propulsion systems. In particular, two-dimensional simulations of liquid sheets should be underway within the next two months. Another interesting two-dimensional problem involves the interaction of a liquid sheet with a transverse gas flow. This flowfield is important to atomization processes in current state-of-the-art gas turbine engine fuel injectors. To perform this calculation, gas flow interactions (such as those discussed in Section 2.2) will need to be incorporated into the model.

Upon the completion of the axisymmetric code, a variety of droplet and liquid jet simulations can be conducted. Droplet-related problems such as secondary atomization and droplet collision/coalescence will be considered. Blanching problems associated with liquid oxygen droplet impact on chamber walls can also be investigated. In addition, a complete simulation of the liquid jet (including internal orifice flow) will be at hand with the completion of the axisymmetric model. This simulation will be useful in gaining knowledge of primary atomization processes which are difficult (if not impossible) to observe experimentally due to the obscuration of this region by the remainder of the spray.

3   Professional Activities

Currently there is one Ph.D. student, Mr. J. H. Hilbing, working on this project. Three masters students; Mr. I. Murray, Mr. M. Moses, and Mr. M. Rutz will be performing related research through funding received in a recently-awarded Augmentation Award for Science and Engineering Research Training (AASERT). As a result of this sponsorship, Mr. C. Spangler recently received his Masters Degree:

Spangler, C.A., "Nonlinear Modeling of Jet Breakup in the Wind-Induced Regime," M.S. Thesis, Purdue University, 1994.

At the present time, two publications (attached in Appendices B and C) have been submitted to referred journals as a result of this research:

Hilbing, J. H., and Heister, S. D., "A Boundary Element Method for Atomization of a Finite Liquid Jet", Submitted to *Atomization and Sprays*, September, 1994.

Spangler, C. A., Hilbing, J. H., and Heister, S. D., "Nonlinear Modeling of Jet Atomization in the Wind-Induced Regime", Submitted to *Physics of Fluids*, August, 1994.

In addition, the authors of these papers attended this year's conference sponsored by the Institute for Liquid Atomization and Spray Systems (ILASS), which was held in Seattle, WA during June, 1994. Both works were presented at this forum; in addition, Professor Heister served as a member of a Panel Discussion on Spray Modeling. These items are summarized below:

Hilbing, J.H., and Heister,, S.D., "A Boundary Element Method for Liquid Jet Atomization Processes", ILASS-94 Conference Proceedings, June 1994.
Spangler, C. A., and Heister, S. D., "Nonlinear Modeling of Jet Atomization in the Wind-Induced Regime", ILASS-94 Conference Proceedings, June, 1994.
Heister, S. D., "Using Boundary Element Methods to Model Atomization Processes", Invited Lecture/ Panel Member, ILASS-94 Tutorial Workshop on Spray Modeling, June, 1994.

Other related work, sponsored by Cummins Engine Company, has been developed during the past year:

Chen, Y and Heister, S. D. A numerical treatment for attached cavitation. to appear in *J. Fluids Engineering* 1994.
Chen, Y. and Heister, S. D. Two-Phase Modeling for Cavitating Flows. *Cavitation and Gas-Liquid Flows in Fluid Machinery and Devices*. FED-Vol. **190** 299-307, 1994.
Chen, Y., and Heister, S. D., "Modeling Hydrodynamic Non-Equilibrium in Bubbly and Cavitating Flows", Submitted to *Journal of Fluid Mechanics*, 1994.

We are currently hoping to use these models to address cavitating orifice experiments recently conducted at Phillips Lab under the supervision of Dr. Doug Talley.

Finally, another manuscript resulting from funding of this research is currently in preparation:

Heister, S. D., "Modeling Gas/Liquid Flows using Boudary Element Methods", to be submitted, *International Journal of Numerical Methods in Fluids*, 1994.

3.1 Technology Transfer/Coupling Activities

This research is rapidly approaching the point at which significant technology transfer and coupling activities will occur. While the goal of this research lies in improving the understanding of atomization processes in connection with combustion instability in liquid rocket engines, the models being developed are quite general in nature and can be applied to many other problems. Examples of commercial applications of interest include: paint sprays, polymer/wax extrusion and manufacturing processes, agricultural sprays, diesel engine injectors, ink jet printers, and fire hoses to name just a few.

There was a significant interest in these modeling efforts at the ILASS meeting attended during June. Not only was the principle investigator invited to serve as a panel member for a tutorial workshop (see above), but numerous industrial officials expressed a strong interest in this work. As a result, we have developed coupling activities with Mr. C. Lipp of Dow Chemical Company and Mr. G. P. Anath of Johnson Wax Corporation. Both of these individuals are eager to apply our future viscous modeling capabilities to industrial manufacturing processes. Officials at Cummins

Engine Company (Dr. W. Eckerle and Dr. S. Menon) are also interested in developments of this modeling capability in connection with injectors for diesel engines. Individuals involved with this research are excited about the industrial applications of this capability and look forward to possible interactions with the industrial officials mentioned above.

4 References

1. Reba, I., and Brosilow, C., "Combustion Instability Liquid Stream and Droplet Behavior. Part III: The Response of Liquid Jets to Large Amplitude Sonic Oscillations," Polytechnic Institute of Brooklyn, WADC Technical Report No. 59-720, Part III, 1960.

2. Jensen, R., (Ed.), "JANNAF Subcommittee on Combustion Stability - Annual Report," 27th JANNAF Combustion Meeting, Cheyenne, Wyoming, 1990.

3. Weber, C., "On the Breakdown of a Fluid Jet", Z.A.M.P., V 11, 1931.

4. Sterling, A. M., and Sleicher, C. A., "The Instability of Capillary Jets", *Journal of Fluid Mechanics*, **68**, 1975, pp. 477-495.

5. Rutland, D.F., and Jameson, G.J., "Theoretical Prediction of the Size of Drops Formed in the Breakup of Capillary Jets", *Chem. Eng. Science*, V 25 p. 1689, 1970.

6. Yuen, M.C., "Non-linear Capillary Instability of a Liquid Jet", *J. Fluid Mech.*, V 34, p. 299, 1968.

7. Przekwas, A. M., Lee, J.-G., Gross, K. W., Chigier, N. A., and Eroglu, H., "Analytical and Experimental Study of Primary Atomization of Water Jets", Fifth International Conference on Liquid Atomization and Spray Systems, Gaithersburg, MD, pp. 831-832, 1991.

8. Sellens, R. W., "A Numerical Model of the Capillary Instability", ILASS-91, July 1991.

9. Mansour, N. N., and Lundgren, T. S., "Satellite Formation in Capillary Jet Breakup", *Physics of Fluids*, V2, pp 1141-1144, 1990.

10. Tjahjadi, M., Stone, H. A., and Ottino, J. M., "Satellite and Subsatellite Formation in Capillary Breakup", *Journal of Fluid Mechanics*, **243**, 1992, pp. 297-317.

11. Hilbing, J.H., and Heister,, S.D., "A Boundary Element Method for Liquid Jet Atomization Processes", ILASS-94 Conference Proceedings, June 1994.

12. Hilbing, J. H., and Heister, S. D., "A Boundary Element Method for Atomization of a Finite Liquid Jet", Submitted to *Atomization and Sprays*, August, 1994.

13. Medina, D. E., "On Droplets and Boundary Elements", Cornell University, FDA-89-12, 1989.

14. Wu, X., and Schelly, Z. A., "The Effects of Surface Tension and Temperature on the Nonlinear Dynamics of the Dripping Faucet", *Physica D*, **40**, pp 433-443, 1989.

15. Spangler, C.A., "Nonlinear Modeling of Jet Breakup in the Wind-Induced Regime," M.S. Thesis, Purdue University, 1994.

16. Spangler, C. A., Hilbing, J. H., and Heister, S. D., "Nonlinear Modeling of Jet Atomization in the Wind-Induced Regime", Submitted to *Physics of Fluids*, August, 1994.

17. Spangler, C. A., and Heister, S. D., "Nonlinear Modeling of Jet Atomization in the Wind-Induced Regime", ILASS-94 Conference Proceedings, June, 1994.

18. Ingber, M. S., and Hailey, C. E., "A Numerical Approach for Modeling Cavitating Flows," *Computational Modeling of Free and Moving Boundary Problems:* Proceedings of the First International Conference, Southampton, U.K., 1991.

19. Wu, J. C., "Boundary Element Solution of Viscous Flow Problems," pp. 1-17 in Boundary Element Te< C. A. Brebbia and W. S. Venturi (ed.), Computational Mathematics Publication, 1987.

20. Kelmanson, M. A., "Boundary Integral Equation Solution of Viscous Flows with Free Surfaces", *Journal of Engineering Mathematics*, Vol. 17, pp. 329-343, 1983.

21. Stone, H. A., and Leal, L. G., "The Influence of Initial Deformation on Drop Breakup in Subcritical Time-Dependent Flows at Low Reynolds Number," *Journal of Fluid Mechanics*, Vol. 206, pp. 223-263, 1989.

22. Camp, C. V., and Gipson, G. S., "A boundary element method for viscous flows at low Reynolds numbers", *Engineering Analysis with Boundary Elements*, Vol. 6, No. 3, 1989, pp. 144-151.

23. The Dual Reciprocity Boundary Element Method, P. W. Partridge, C. A. Brebbia, and L. C. Wrobel, Computational Mechanics Publications, Southampton, 1992

24. Nowak, A. J., and Partridge, P. W., "Comparison of the dual reciprocity and the multiple reciprocity methods", *Engineering Analysis with Boundary Elements*, Vol. 10, 1992 pp. 155-160.

25. Jin, X., and Brown, D. K., "Dual Reciprocity BIE in Lagrangian Form for Incompressible Unsteady Viscous Flow", *Boundary Element Technology, Ed., C. A. Brebbia*, 1991.

26. Kamiya, N., and Nakayama, K., "Prediction of Free Surface Die Swell Using the Boundary Element Method", *Computers and Structures*, Vol. 46, pp. 387-395, 1993.

27. Jin, X., "Boundary Element Study on Particle Orientation Caused by the Fountain Flow in Injection Molding", *Polymer Engineering and Science*, Vol. 33, pp. 1238-1242, 1993.

28. Partridge, P. W., and Brebbia, C. A., "Computer Implementation of the BEM Dual Reciprocity Method for the Solution of General Field Equations", *Communications in Applied Numerical Methods*, Vol. 6, pp. 83-92, 1990.

Appendix A

Documents Related to Four Month No Cost Contract Extension

PURDUE UNIVERSITY

SCHOOL OF AERONAUTICS
AND ASTRONAUTICS

May 23, 1994

Dr. Mitat A. Birkan
AFOSR/NA
110 Duncan Avenue, Suite B115
Bolling AFB, Washington, D.C. 20332-0001

Dear Dr. Birkan:

As you know, our current AFOSR contract (F49620-92-J-0390) expires on 30 June, 1994. I would like to request a four month extension on this contract. Since the original funding started in the summer, I was not able to obtain a graduate student until the following January (1 January, 1993) which delayed spending on salaries by about six months. While we have made up part of the difference due to this offset, an additional four months is required to account for this delay. Finally, I should note that as far as I am concerned we can still support the same reporting requirements on the Final Technical Report (due 31 August, 1994). However, the Final Fiscal Report (currently due on 30 September, 1994) would have to be delayed since the extended contract would not have been completed at that time.
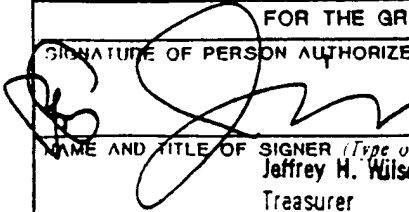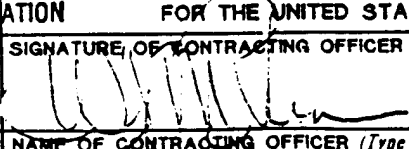
Please give me a call at 317-494-5126 if I can be of further assistance in this matter.

Yours truly,

Stephen D. Heister
Assistant Professor

GRANT AMENDMENT
UNITED STATES AIR FORCE
AIR FORCE OFFICE OF SCIENTIFIC RESEARCH
BUILDING 410, BOLLING AFB, D. C. 20332-0001

GRANT NO.	AMEND	EFFECTIVE DATE	PURCHASE REQUEST NO.	PROJECT-TASK	
F49620-92-J-0390	P00001	01 Jul 94	N/A	2308/AS	PAGE 1 OF 1

GRANTEE	AUTHORITY 10 U.S.C. 2358
Purdue Research Foundation Hovde Hall 3rd Floor West Lafayette IN 47907-0199 AFOSR's CFDA #12.800	**CHANGE IN GRANT AMOUNT** N/C **CHANGE IN DURATION** 4 months

ADMINISTRATIVE OFFICE	SPONSORING SCIENTIFIC OFFICE	PAYING OFFICE
AFOSR/PKA 110 Duncan Avenue Suite B115 Bolling AFB DC 20332-0001	AFOSR/NA 110 Duncan Avenue Suite B115 Bolling AFB DC 20332-0001	DAO-DE AFDW/FS (202) 767-4736 170 Luke Avenue Suite 280 Bolling AFB DC 20332-5113

NEGOTIATOR (Name, Organization, Telephone No.)	PROGRAM MANAGER (Name, Organization, Telephone No.)
Karen Buck/PKA (202) 767-6838	Dr. Mitat A. Birkan/NA (202) 767-4987

ACCOUNTING AND APPROPRIATION DATA

N/C

THE GRANT IDENTIFICATION ABOVE IS MODIFIED AS FOLLOWS:

By changing the addresses for the Administrative Office, Sponsoring Scientific Office and Paying Office as indicated above.

By changing the grant duration from 24 to 28 months and establishing an expiration date of 31 Oct 94.

The following reports shall be submitted to the Administrative Contracting Officer, AFOSR/PKA on the dates and in the quantities shown below:

REPORTS	PERIOD COVERED	DUE DATE	NUMBER OF COPIES
Annual Technical	1 Jul 92 - 30 Jun 93	31 Jul 93	6
Annual Invention	1 Jul 92 - 30 Jun 93	31 Aug 93	3
Annual Fiscal	1 Jul 92 - 30 Jun 93	30 Sep 93	2
Final Technical	1 Jul 92 - 31 Oct 94	31 Dec 94	6
Final Invention	1 Jul 93 - 31 Oct 94	30 Apr 95	3
Final Fiscal	1 Jul 93 - 31 Oct 94	31 Jan 95	2

EXCEPT AS PROVIDED WHEREIN, ALL TERMS AND CONDITIONS OF THE GRANT, AS HERETOFORE CHANGED, REMAIN UNCHANGED AND IN FULL FORCE AND EFFECT.

FOR THE GRANTEE PURDUE RESEARCH FOUNDATION	FOR THE UNITED STATES OF AMERICA
SIGNATURE OF PERSON AUTHORIZED TO SIGN	SIGNATURE OF CONTRACTING OFFICER

| NAME AND TITLE OF SIGNER (Type or Print)
Jeffrey H. Wilson
Treasurer | DATE SIGNED
AUG 2 1994 | NAME OF CONTRACTING OFFICER (Type or Print)
WENDY M. VEON
Administrative Contracting Officer | DATE SIGNED
11 Aug 94 |

AFSC FORM JUL 84 454   (Computer Generated)

Appendix B

Manuscript Submitted to Physics of Fluids

Nonlinear modeling of jet atomization in the wind-induced regime

Christopher A. Spangler, James H. Hilbing, and Stephen D. Heister

Department of Aeronautics and Astronautics, Purdue University, West Lafayette, Indiana 47906

Abstract

A Boundary Element Method (BEM) has been developed to solve for the nonlinear evolution of a liquid jet acting under the influence of both surface tension and the aerodynamic interactions with the surrounding atmosphere. For longer waves, aerodynamic effects are shown to cause a "swelling" of the liquid surface in the trough region. The model predicts the presence of satellite drops in the first wind-induced regime, and predicts the evolution of a "spiked" surface at the periphery of the jet for conditions consistent with the second wind-induced regime. The effects of the disturbance wave number, the liquid Weber number, and the density ratio between the liquid jet and the surrounding gas on the breakup of the jet have been examined. Transition points between various flow regimes have also been identified.

I. Introduction

The atomization of a liquid jet in a gaseous environment is a fundamental problem in two-phase flows. The numerous applications of this flow include devices used for liquid fuel injection systems, spray painting, and ink jet printing. Reitz and Bracco[1] developed a classification of liquid jet atomization regimes as highlighted in Fig. 1. The Rayleigh and first wind-induced regimes are characterized by the formation of drops with diameters larger than that of the orifice. The breakup in the Rayleigh regime is governed solely by capillary instabilities, while in the first wind-induced regime, the capillary instabilities are enhanced by the aerodynamic interactions with the surrounding gas. For the second wind-induced and atomization regimes, the breakup is characterized by the formation of drops significantly smaller than the jet diameter. In this case, the wave formation is driven by aerodynamic forces since surface tension serves as a stabilizing force for the shorter waves formed in this regime. In the atomization regime, the drops are formed very near the orifice exit plane and viscous effects are known to be of great importance.

The theoretical basis for the capillary instability was first investigated by Rayleigh,[2] who conducted a linear analysis neglecting the effect of gas pressure variations on jet distortion. Weber[3] developed a linear theory similar to Rayleigh's, but he included the effects of both the liquid viscosity and the pressure of the surrounding gas on the jet behavior. The effect of variations in gas velocity was later incorporated into a linear analysis by Sterling and Sleicher.[4] By considering higher-order terms in an expansion of the surface deformation or jet velocity, more recent efforts[5-7] have been able to improve on predicted surface distortions due to the capillary instabilities in the absence of gas-phase pressure variations. These works predicted that a single wave would divide into two droplets (called main and satellite drops) as opposed to the single drop predicted by the linear theory.

Experimental measurements of flows consistent with the Rayleigh regime[7-10] confirmed the presence of satellite drops formed during the nonlinear portion of the atomization process. These experiments were performed by using a forced oscillation frequency thus permitting investigation of the growth of instabilities over a range of wavelengths. More recently, experimental efforts have also focused on the control of the satellite size through the use of higher harmonics of the forcing frequency[11,12] as well as amplitude modulation[13] techniques.

Unfortunately, very few experiments have been reported at conditions consistent with the first wind-

17

induced regime. While some efforts have focused on jet breakup length,[4,9] very few droplet size measurements have been made at moderate jet velocities consistent with the first wind-induced regime. The influence of viscosity on the breakup of a liquid jet was examined by Goedde and Yuen.[10] They found that viscosity served as a stabilizing influence on the growth rate. They also noted that the pressure field around the liquid jet has an influence on the formation of droplets although they did not quantify this effect. Rutland and Jameson[14] examined the occurrences of secondary swellings between the primary crests of a liquid jet.

Most recently, Mansour and Lundgren[15] developed a full nonlinear simulation of the Rayleigh breakup process utilizing a boundary element method (BEM). The use of a BEM is attractive in flows of this nature because of the high accuracy these techniques provide in assessing curvature of highly deformed surfaces. This feature is crucial in flows in which capillary forces play a substantial role. This work presents an extension of the model due to Mansour and Lundgren for the case where gas-phase pressure variations are not negligible. The model, based on a BEM approach, is discussed in the following section. Comparisons are made for both linear theory and measured drop sizes, and detailed surface evolutions are presented as well.

II. Model Development

In developing the model, we assume that the flow is inviscid and incompressible, and that no gravity or other body forces are present. Under these assumptions, the unsteady liquid and gas behavior is described by Laplace's equation $\nabla^2\phi = 0$ where ϕ is the velocity potential such that its gradient is simply the velocity, $\nabla \cdot \phi = \vec{v}$. We also assume that finite disturbances of a periodic nature develop well downstream of the jet orifice such that the evolution of the jet is accurately represented as an infinite wavetrain. This assumption removes the influence of the orifice on the evolution of the jet surface.

For this analysis, the characteristic dimensions utilized are the unperturbed jet radius, the mean jet velocity, and the liquid density. Under this nondimensionalization, the governing equations indicate that the Weber number and gas/liquid density ratio are the appropriate dimensionless variables characterizing this flow. We define the Weber number as: $We = \rho_\ell U^2 a/\sigma$, where ρ is the liquid density, U is the relative velocity between the liquid and gas, a is the orifice radius, and σ is the surface tension. Also, the density ratio is: $\epsilon = \rho_g/\rho_\ell$ where ρ_g is the gas density. The nondimensional form of the Bernoulli equation relates

velocity potentials to the local pressure at the interface. In the liquid region, this condition is expressed:

$$\frac{\partial \phi}{\partial t} + \frac{1}{2}(\nabla \phi)^2 + P_g + \frac{\kappa}{\text{We}} = 0 \tag{1}$$

while in the gas region it is:

$$\epsilon \frac{\partial \phi_g}{\partial t} + \frac{\epsilon}{2}(\nabla \phi_g)^2 + P_g = 0 \tag{2}$$

where κ is the surface curvature and P_g is the gas pressure on the surface. These two equations are boundary conditions on the interface and are coupled through the local gas pressure. This coupling must be addressed in the development of a consistent, stable integration procedure.

Figure 2 depicts the computational domain, coordinate system, and boundary conditions utilized in the calculations. In this figure, ϕ_g represents the velocity potential in the gas phase, q represents the velocity normal to the local surface, and the radial and axial coordinates are denoted r, z, respectively. Nodes are placed along the interface, along vertical planes at both ends of the wave, and along a horizontal surface, in the gas, far from the interface. The liquid nodes are denoted "o", while the gas nodes are denoted "x". The initial wave shape of the surface is assumed to be:

$$r = 1 + \eta \cos(kz) \tag{3}$$

where η is the initial surface deflection and k is the wave number of the forcing disturbance on the jet. The solution procedure employed requires an initial prediction for both the pressure, P_g, on the wave surface and ϕ_g along the surface, which are determined from the potential flow solution for flow over a wavy cylinder[16]:

$$P_g = -\epsilon \eta k \cos(kz) \frac{K_0(kr)}{K_1(k)} \tag{4}$$

$$\phi_g = z - \eta \sin(kz) \frac{K_0(kr)}{K_1(k)} \tag{5}$$

where K_0 and K_1 are modified Bessel functions of the second kind. The ends of the gas domain are gridded using an exponential stretching technique to reduce the total number of nodes on these surfaces, while retaining the higher accuracy of the finer mesh near the interface. The uppermost boundary in the gas phase is place ten radii from the centerline. Numerical experiments indicate that this distance is adequate to apply the $q = 0$ boundary condition without adverse effects on the behavior of the interface. Nodes are initially placed with equal spacing along all surfaces associated with the liquid domain.

The Boundary Element Method is used to develop a computational model to predict the nonlinear evolution of the jet surface in time[17]. The formulation of the BEM starts with the integral representation of Laplace's equation. Following Liggett and Liu[18], this is:

$$\alpha\phi(\vec{r_i}) + \int_\Gamma \left[\phi\frac{\partial G}{\partial \hat{n}} - qG\right] d\Gamma = 0 \tag{6}$$

where $\vec{r_i}$ denotes the vector from the origin to point "i", $\phi(\vec{r_i})$ is the value of the potential at this point, Γ denotes the boundary of the domain, and G is the free space Green's function. For the BEM, either ϕ or $q = \partial\phi/\partial\hat{n}$ is specified at each "node" on the boundary. Here $\hat{n}$ is the outward normal to the boundary such that q is the velocity normal to the boundary. The quantity α in Eq. 6 results from singularities introduced as the integration passes over the boundary point, $\vec{r_i}$. For the axisymmetric formulation, α is related to the angle between successive nodes on the boundary. The free space Green's function solution to the axisymmetric Laplacian is[18]:

$$G = \frac{4rK(p)}{\sqrt{a}} \tag{7}$$

with

$$a = (r + r_i)^2 + (z - z_i)^2 \qquad p = \frac{(r - r_i)^2 + (z - z_i)^2}{(r + r_i)^2 + (z - z_i)^2} \tag{8}$$

where $K(p)$ is the complete elliptic integral of the first kind.

Physically, the free space Green's function represents the influence of a source at location $\vec{r}$ of strength 2π on the "base point", $\vec{r_i}$. While the quantity $\partial G/\partial\hat{n}$ represents the influence of a doublet at location $\vec{r}$ on the base point. By properly weighting all these source and doublet strengths, Laplace's equation can be solved for arbitrary boundary conditions. Derivation of $\partial G/\partial n$ for this axisymmetric problem is quite involved. Gipson[19] gives:

$$\frac{\partial G}{\partial n} = \frac{-1}{2\sqrt{a}}\left[\hat{n}_r K(p) + \frac{E(p)}{(r-r_i)^2 + (z-z_i)^2}\left[\left((r-r_i)^2 - (z-z_i)^2\right)\hat{n}_r + 2r\hat{n}_z(z-z_i)\right]\right] \tag{9}$$

with the quantities $\hat{n}_r$ and $\hat{n}_z$ being the components of the outward normal unit vector in the radial and axial directions, respectively, while $E(p)$ is the complete elliptic integral of the second kind.

Performing the desired integration around the boundary of the domain results in an algebraic system of equations. In order to perform this integration, a linear element formulation is employed in which ϕ, ϕ_g, and q are assumed to have a linear variation between successive nodes. With this assumption, the values for the

20

potential of the element bounded by nodes j and $j + 1$ is:

$$\phi = \phi_j \frac{\Gamma_{j+1} - \Gamma}{\Gamma_{j+1} - \Gamma_j} + \phi_{j+1} \frac{\Gamma - \Gamma_j}{\Gamma_{j+1} - \Gamma_j} \tag{10}$$

with analogous expressions for ϕ_g and q. Using linear elements, Eq. 6 is divided into two separate integrals:

$$\int_\Gamma q G d\Gamma = \sum_{j=1}^{n-1} [q_j I_1(i,j) + q_{j+1} I_2(i,j)] \tag{11}$$

and

$$\int_\Gamma \phi \frac{\partial G}{\partial n} d\Gamma = \sum_{j=1}^{n-1} [\phi_j I_3(i,j) + \phi_{j+1} I_4(i,j)] \tag{12}$$

where

$$I_1 = \int_{\Gamma_j}^{\Gamma_{j+1}} \frac{\Gamma_{j+1} - \Gamma}{\Gamma_{j+1} - \Gamma_j} G d\Gamma \qquad I_3 = \int_{\Gamma_j}^{\Gamma_{j+1}} \frac{\Gamma_{j+1} - \Gamma}{\Gamma_{j+1} - \Gamma_j} \frac{\partial G}{\partial n} d\Gamma \tag{13}$$

$$I_2 = \int_{\Gamma_j}^{\Gamma_{j+1}} \frac{\Gamma - \Gamma_j}{\Gamma_{j+1} - \Gamma_j} G d\Gamma \qquad I_4 = \int_{\Gamma_j}^{\Gamma_{j+1}} \frac{\Gamma - \Gamma_j}{\Gamma_{j+1} - \Gamma_j} \frac{\partial G}{\partial n} d\Gamma \tag{14}$$

The integrals I_1 through I_4 are calculated using four point Gaussian Quadrature, and are used to create D and S matrices which contain doublet and source contributions, respectively. Since G and $\partial G / \partial n$ are singular when the integration passes over the base point, special treatment of the integrals in Eqs. 13 and 14 is used for these cases[17]. From Eqs. 11 and 12, we can write:

$$S_{i,j} = I_{1_{i,j}} + I_{2_{i,j-1}} \qquad D_{i,j} = I_{3_{i,j}} + I_{4_{i,j-1}} \tag{15}$$

so that the integration of Eq. 6 results in a system of algebraic equations of the form:

$$[D]\{\phi\} = [S]\{q\} \tag{16}$$

with the values of α incorporated into diagonal elements of the D matrix. To solve this system of equations, all the unknown terms are "pivoted" by interchanging the columns of the appropriate matrices, giving the standard form for a linear system of equations. The system is fully populated and is solved by an LU decomposition method.

The boundary conditions on the interface between the liquid and the gas are the Bernoulli equations in the two domains. Nodes on the interface are assumed to travel with the local liquid surface velocity, so a transformation from the Eulerian to Lagrangian reference frame is required. After this transformation, Eqs. 1 and 2 become:

$$\frac{D\phi}{Dt} = \frac{1}{2} (\nabla \phi)^2 - P_g - \frac{\kappa}{\text{We}} \tag{17}$$

$$P_g = -\frac{\epsilon}{2}(\nabla\phi_g)^2 - \epsilon\frac{D\phi_g}{Dt} + \nabla\phi \cdot \nabla\phi_g \qquad (18)$$

In these expressions, the notation D/Dt denotes changes in time for nodes moving with the liquid interfacial velocity.

The procedure to solve these two equations is as follows: At the beginning of each time step, an initial value of ϕ is known. Using this value of ϕ as the boundary condition on the interface, solution of Laplace's equation in the liquid domain provides values of q on the interface. The interfacial velocity is then used as a boundary condition for the gas phase solution of Laplace's equation. Using this value of q, the ϕ_g value on the gas side of the interface is obtained. The new value of the gas velocity potential in Eq. 18 allows a new gas pressure to be calculated by approximating $D\phi_g/Dt$ using a first order backward difference in time. The new gas pressure is then put into Eq. 17 to determine the change in ϕ with time.

Nodes on the surface are moved by integration of the kinematic boundary conditions:

$$\frac{Dr}{Dt} = \frac{\partial\phi}{\partial r} \qquad\qquad \frac{Dz}{Dt} = \frac{\partial\phi}{\partial z} \qquad (19)$$

Each time ϕ is updated, Eqs. 19 are integrated to determine the motion of nodes on the interface using a fourth-order Runge Kutta method. The velocities $\partial\phi/\partial r$, $\partial\phi/\partial z$ are obtained from a coordinate transformation:

$$\frac{\partial\phi}{\partial r} = \frac{\partial\phi}{\partial s}sin\beta + qcos\beta \qquad (20)$$

$$\frac{\partial\phi}{\partial z} = \frac{\partial\phi}{\partial s}cos\beta - qsin\beta \qquad (21)$$

Here, s is a natural coordinate aligned with the surface. The velocity tangential to the surface, $\partial\phi/\partial s$, is obtained from a fourth-order centered difference approximation. The quantity β represents the local angle of the surface with respect to the horizontal direction. This angle is determined by fitting a parabola through the point in question and its nearest neighbors. Surface curvatures are obtained by utilizing a fourth-order, centered difference formula.

Since the nodes on the interface are allowed to move with their local velocity, over time they tend to group themselves in the center of the jet. This grouping of the nodes is undesirable as it leaves the ends of the interface poorly defined. To alleviate this problem, the surface mesh is regridded using a series of cubic splines (for r, z, ϕ, and ϕ_g) at each time step to keep the spacing between the nodes constant across the surface. The use of the Runge-Kutta integration scheme is well suited to this remeshing scheme, since it

does not require information on node positions at previous time levels to predict the subsequent motion of the surface.

A special treatment is required for nodes on each end of the interface because the outward normal vector is multivalued at these corners in the domain. In the liquid domain, we have $q = 0$ in the axial direction due to the periodic boundary condition, so that the node is tracked vertically. In the gas domain, the axial velocity is lagged one time step and the vertical velocity is obtained from the liquid domain solution. Using these two velocity components at the corner permits the solution of ϕ_g at this location.

As the interface deforms over time, eventually it will reach the centerline of the domain. Physically, at this time, the jet pinches into a series of distinct droplets. Numerically, to prevent a node from obtaining a negative radius, the jet is considered "pinched" when any node on the surface comes within a distance of 1% of the initial jet radius of the centerline. At this time, the jet is broken into discrete drops, and their volume and radii are calculated. The radii of these drops has been found to be insensitive to this assumed pinch criteria.

III. Model Validation

The model has been validated through comparisons with previous experimental and computational studies. By assuming a very small initial wave height, comparisons can be made with the linear theory developed by Sterling and Sleicher.[4] Figure 3 depicts the growth rate comparison as a function of disturbance wave number for different Weber numbers at a density ratio of 0.001, approximately that of ambient air surrounding a water jet. Errors of less than 1% are achieved using grids involving as few as 59 nodes along the interface. The different Weber numbers examined correspond to breakup in the Rayleigh regime (We = 2), the first wind-induced regime (We= 1500), and the second wind-induced regime (We = 15,000).

The initial surface deflection (η) was assumed to be 0.001 for these calculations. It is interesting to note that substantial differences between nonlinear calculations and linear theory occur even for η values as small as 0.01. This result indicates that nonlinear behavior can be affected by relatively small perturbations induced by some mechanical device with a minimal energy input. Various researchers have capitalized on this behavior in controlling droplet sizes experimentally by using frequency modulation[11,12] or through amplitude and frequency modulation.[13]

Nonlinear attributes of the calculation were validated by comparison with similar predictions of Mansour

and Lundgren[15], as well as experimental measurements of Rutland and Jameson.[14] The comparison to the nonlinear surface shape calculated by Mansour and Lundgren[15] is not presented here in the interest of brevity. When the current model is run for the same conditions (We $= 2$, $\epsilon = 0.0, k = 0.3, 0.6$) both the nonlinear surface shapes and the predicted peak and trough growth rates are are identical. In addition, convergence studies, carried out on grids of various sizes, indicate a second-order convergence rate consistent with the linear elements used in the BEM implementation.

A comparison has also been generated for highly-distorted surface shape measurements of Rutland and Jameson.[14] Figure 4 provides the comparison between the experimental wave shape reported by Rutland and Jameson and that calculated by the BEM. Two different density ratios ($\epsilon = 0; 0.00129$) are examined for We $= 109.6$; half a wavelength of the surface is plotted. Calculation of the volume of fluid present in the Rutland and Jameson result indicate a slightly lower wave number ($k = 0.237$) than that quoted ($k = 0.25$). This difference could easily be attributed to "accordion effects" of wave stretching due to the fact that the domain is in fact finite. Using $k = 0.237$, results in Fig. 4 were obtained by matching the height of the crest and plotting the resulting waveform. The results indicate that even at the relatively low We value, aerodynamic interactions with the gas phase are important in determining the nonlinear wave shapes. The "swelling" in the trough region of the experimental data is also predicted for the $\epsilon = 0.00129$ case using the present model, although not to the extent measured by Rutland and Jameson. Nevertheless, the result including aerodynamic effects is clearly superior to the calculation ignoring gas presence. Errors between the $\epsilon = 0.00129$ result and the experiment can be attributed to the nonperiodicity of the actual measurement as well as viscous effects.

IV. Results and Discussion

Results of calculations using the model are shown in Figs. 5-11. Figure 5 presents a typical growth rate for the surface. In this figure the square of the growth rate (ω) is plotted versus the nondimensional time for two locations on the jet surface for We $= 850$, $\epsilon = 0.00129$, $k = 1.07$, and 89 nodes along the jet surface. The growth rate is plotted for both the initial peak ($kz = 0$) and the initial trough ($kz = \pi$) of the disturbance along with the value predicted by the linear theory. The computed growth rates for both the peak and the trough agree very well with the linear theory for about the first 250 time increments. At this point, the growth of the jet departs from the linear theory and becomes nonlinear. The growth rate of the

trough dramatically decreases once the jet is in the nonlinear portion of the process, and it is this decrease in the growth rate of the trough (equivalent to a decrease in the radial velocity of the trough) that leads to the formation of the main and the satellite drops. If the trough did not undergo this decrease in the growth rate, the jet would form only one droplet per wavelength when it pinched. The "wiggles" on the growth rates during the first 50 time increments are a result of the method of treating the corner nodes in the gas domain. The magnitude of these oscillations is reduced by increasing the number of nodes along the wave, or decreasing either the initial time step the initial disturbance amplitude. The presence of these oscillations has a negligible impact on either the breakup length of the jet or on the drop sizes formed.

Figure 6 presents the nonlinear jet evolution in the first wind-induced regime. This plot is for the same conditions as the growth rate plot (Fig. 5). In this figure, the surface shape is given at three different time steps during the evolution, with two complete waves of the disturbance shown. The first surface shape is at $t = 250$, and corresponds to a point just after the jet enters into the nonlinear portion of its growth. At this point, the maximum and the minimum radii of the surface are at the points that correspond to the initial peaks and troughs of the wave. The second surface shape is given at $t = 300$, well into the nonlinear portion of the jet growth. At this time, the minimum radius point on the surface no longer corresponds to the initial trough. The trough area has flattened out and there are now two points of minimum radius per wavelength, one at each end of the flattened trough area. The final surface shape shown is for $t = 312$, just before the pinching process occurs. At this time, the larger main drops are separated by thin ligaments of fluid that make up the satellite drops. The swelling phenomena is not as pronounced as that in Fig. 4 for this relatively short wavelength disturbance.

Using this model, we have identified the region in which jet breakup transitions from the first to second wind-induced regimes. Figure 7 gives the nonlinear jet evolution for the transition region for We = 1800, $\epsilon = 0.00129$, $k = 1.68$, and 79 nodes on the interface. Again, the jet surface is shown at three different times during its evolution. The evolution of the trough through the times shown is similar to the trough in the first wind-induced regime. The evolution of the peak however, is significantly different than it is for the first wind-induced case. At $t = 200$, the peak is still rounded. As the surface evolves to $t = 225$, the peak loses its rounded shape and takes on more of a "peaked" appearance. Between $t = 225$ and $t = 241$, the peak undergoes even a more dramatic change in appearance. The peak loses all of the rounded shape and it

now forms a "ring" type structure around the edge of the jet. It is the formation of this ring structure that leads to droplet shedding from the periphery of the jet in the second wind-induced region. When the jet pinches in this transition regime, the satellite drops still have the same appearance as they did in the first wind-induced regime, while the main drops are no longer spherical and are drawn out into a "ring" around the edge of the jet.

The nonlinear jet evolution in the second wind-induced regime is given in Figure 8 for We = 5000, $\epsilon = 0.00129$, $k = 4.23$, and 89 nodes on the interface. In this figure, the jet surface shape is given at four different times during its evolution. The evolution of the surface shape is significantly different than it was for the lower Weber number jets. At the first time shown ($t = 50$), the jet has undergone almost no motion of the surface and is still sinusoidal. At $t = 80$, the surface still appears sinusoidal although the peak has started pulling outward. At $t = 90$, the peak has acquired a spiked shape and is moving outward with a rapid velocity. When the jet pinches at $t = 100$, the peak has pulled up a significant distance from the surface and has a definite "ring" structure at the edge. When this ring of fluid is shed from the periphery of the jet, the trough is not close to the centerline of the jet. Once the ring of fluid is shed, it will further break up into a series of smaller drops around the edge of the jet, and these small drops are characteristic of the second wind-induced regime.

At this point, it is prudent to caution the reader of the effects of gas-phase viscosity on the predictions in Figs. 6-8. The most important real fluid effect is the flow separation which will undoubtedly occur in the highly-distorted shapes obtained at large times. The net drag force induced by this flow separation (F_D) can be expressed in terms of the dynamic pressure and the height of the wave:

$$F_D \propto \rho_g U^2 \eta \tag{22}$$

whereas, the net force generated due to surface tension at the interface is:

$$F_\sigma \propto \sigma \tag{23}$$

so that viscous effects will become important as the ratio:

$$F_D/F_\sigma \approx \epsilon \mathrm{We} \frac{\eta}{a} \tag{24}$$

approaches unity. This condition is roughly attained at times t=300, 200, and 80, respectively, in Figs. 6-8. Beyond these times, we expect a noticible deflection of the peaks in the downstream direction for the

case of a viscous fluid. However, we note that gas separation is not an essential mechanism to explaining the gas/liquid interaction, particularly at conditions where the ratio F_D/F_σ is small compared to unity. A complete viscous analysis would be quite demanding computationally, since we could no longer employ periodic boundary conditions due to differences in boundary layer thickness at either end of a given wave.

Figure 9 compares the drop sizes predicted by the model with those measured by Rutland and Jameson[8] and Lafrance[7]. Unfortunately, all of these data lie well within the Rayleigh regime; we were unable to find analogous measurements at higher jet velocities. Our calculations slightly underpredict the size of the main drops, resulting in a corresponding overprediction of the satellite drop sizes. This result is essentially the same as that calculated by Mansour and Lundgren (with the exception that actual gas density and jet velocity were used for each datapoint) due to the fact that low speed jets were utilized in generating the data. There were some subtle differences obtained by including gas phase interactions, but in general these differences were of the order of 1-2% in droplet diameters.

Figure 10 depicts the radius of the main and the satellite drops versus the wave number of the disturbance for $\epsilon = 0.00129$ and We = 2, 850, and 1500. For We = 2, the main and satellite drops are of equal size for $k = 0.28$. Below this wave number, the satellite drops are larger than the main drops, while above this wavenumber, the main drops are larger than the satellite drops. At increased jet velocities (i.e. Weber numbers), the main drop radius decreases and the satellite drop correspondingly increases in size. This effect is attributed to the importance of the swelling phenomena described in Fig. 4. At higher We values, the swelling in the trough region is more dramatic (particularly for lower k values), thus moving the pinch location closer to the peak and increasing the size of the satellite droplet.

A series of calculations were performed at various density ratios in order to identify the the transition point between the flow regimes. The transition between the Rayleigh and the first wind-induced regimes occurs at the longest breakup length jet. Using a linear analysis, one can show that aerodynamic forces are of the same order as the capillary force when the gas-based Weber number (We$_g$) is equal to unity. This condition corresponds to the transition between Rayleigh and first wind-induced regimes. The transition between first and second wind-induced regimes is only evident under large deformations and can only be predicted using a complete nonlinear analysis. This transition is important since it signals the point at which atomization occurs at the jet periphery, rather than at the centerline.

27

Figure 11 shows results of the transitions studies in terms of a the jet breakup length versus We_g for various ϵ values. For each density ratio, the transition point between the Rayleigh and the first wind-induced regimes occurs at $We_g = 1.0$, as predicted by linear theory. This point corresponds to the maximum breakup length of the jet as depicted in Fig. 11. Agreement with the linear result $We_g = 1$ is not surprising, since the growth rate is near the linear result for the bulk of the process (e.g. Fig. 5).

For a given density ratio, We_g was increased to the point where atomization began to occur at the periphery of the jet. This point, noted by the termination of each of the curves in Fig. 11, signals transition from the first to the second wind-induced regimes. Results indicate that this transition occurs at $We_g \approx 2.5$ over the large range of density ratios studied. Figure 11 also shows the effect of increasing the density ratio on the breakup length of the jet. As density ratio increases, the aerodynamic forces become more important, and the jet becomes more unstable and has a shorter length upon breakup as suggested by the linear theory.

VII. Conclusions

Nonlinear atomization processes have been modeled for a liquid jet under the influence of both capillary forces and aerodynamic interactions with an external gas. The model is capable of predicting the nonlinear evolution of the gas/liquid interface within both wind-induced regimes. Validations against linear theory suggest adequate agreement in the case where initial jet deflections are assumed to be 0.1% of the initial jet radius. Significant nonlinear effects are present for initial deflections as small as 1% of the jet radius. Comparison with highly distorted surface shape measurements indicate that the gas phase interaction is important even at relatively low jet velocities. The presence of the gas leads to a "swelling" in the trough region of the wave which is predicted by the current model. Aerodynamic interactions had very little effect on predicted droplet sizes for low speed jets within the Rayleigh regime. At higher velocities, a decrease in main drop size (with an attendant increase in satellite drop size) is predicted by the model. This behavior is attributed to the swelling phenomena which effectively drives the pinch location toward the main droplet at higher jet velocities. Results also indicate that transitions from Rayleigh to first wind-induced and from first to second wind induced regimes occur at $We_g = 1$ and $We_g \approx 2.5$, respectively.

Acknowledgments

References

[1] R. D. Reitz and F. V. Bracco, "Mechanisms of atomization of a liquid jet," Phys. Fluids **25**, 1730 (1982).

[2] W. S. Rayleigh, "On the instability of jets," Proc. London Math. Soc. **10**, 4 (1878).

[3] C. Weber, "'On the breakdown of a fluid jet," Z. Agnew. Math. Mech. **11**, 136 (1931).

[4] A. M. Sterling and C. A. Sleicher, "The instability of capillary jets," J. Fluid Mech. **68**, 477 (1975).

[5] M. C. Yuen, "Non-linear capillary instability of a liquid jet," J. Fluid Mech. **33**, 151 (1968).

[6] K. C. Chaudhary and L. G. Redekopp, "The nonlinear capillary instability of a liquid jet. part 1. theory," J. Fluid Mech. **96**, 257 (1980)

[7] P. Lafrance "Nonlinear breakup of a laminar liquid jet," Phys. Fluids **18**, 428 (1975).

[8] D. F. Rutland and G. J. Jameson, "Theoretical prediction of the sizes of drops formed in the breakup of capillary jets," Chem. Eng. Sci. **25**, 1689 (1970).

[9] R. W. Fenn III and S. Middleman, "Newtonian jet stability: the role of air resistance," AIChE J. **15**, 379 (1969).

[10] E. F. Goedde and M. C. Yuen, "Experiments on liquid jet instability," J. Fluid Mech. **40**, 495 (1970).

[11] K. C. Chaudhary and T. Maxworthy, "The nonlinear capillary instability of a liquid jet. part 2. experiments on jet behavior before droplet formation," J. Fluid Mech. **96**, 275 (1980).

[12] K. C. Chaudhary and T. Maxworthy, "The nonlinear capillary instability of a liquid jet. part 3. experiments on satellite drop formation and control," J. Fluid Mech. **96**, 287 (1980).

[13] M. Orme and E. P. Muntz, "The manipulation of capillary stream breakup using amplitude-modulated disturbances: a pictorial and quantitative representation," Phys. Fluids A **2**, 1124 (1990).

[14] D. F. Rutland and G. J. Jameson, "A non-linear effect in the capillary instability of liquid jets," J. Fluid Mech. **46**, 267 (1971).

[15] N. N. Mansour and T. S. Lundgren, "Satellite formation in capillary jet break-up," Phys. Fluids A **2**, 1141 (1990).

[16] W. R. Sears, *Small Perturbation Theory* (Princeton University Press, 1960).

[17] J. H. Hilbing and S. D. Heister, "A boundary element method for atomization of a finite liquid jet," Atomization and Sprays (in review).

[18] J. A. Liggett and P. L.-F. Liu, *The Boundary Integral Equation Method for Porous Media Flow* (Allen and

Unwin, London, 1983).

[19]G. S. Gipson, in C. A. Brebbia and J. J. Conner (eds.), *Boundary Element Fundamentals, Topics in Engineering, Volume 2* (Computational Mechanics Publications, 1987).

Figure Captions

FIG. 1. Regimes of Jet Breakup: a) Rayleigh, b) First Wind-Induced, c) Second Wind-Induced, d) Atomization

FIG. 2. Schematic of Computational Domain Denoting Boundary Conditions

FIG. 3. Comparison of BEM to Linear Theory for $\epsilon = 0.001$ and (a) We = 2, 1500 and (b) We = 15,000

FIG. 4. Comparison to Wave Shapes of Rutland and Jameson[14], $k = 0.237$, We = 109.6, $\epsilon = 0.0$, 0.00129

FIG. 5. Growth Rate for the Initial Peak and Trough in the First Wind-Induced Regime, $\epsilon = 0.00129$, $\eta = 0.004$, $k = 1.07$, We = 850

FIG. 6. Nonlinear Jet Evolution in the First Wind-Induced Regime, $\epsilon = 0.00129$, $k = 1.07$, $\eta = 0.004$, We = 850

FIG. 7. Nonlinear Jet Evolution in the Transition Region, $\epsilon = 0.00129$, $\eta = 0.01$, $k = 1.68$, We = 1800

FIG. 8. Nonlinear Jet Evolution in the Second Wind-Induced Regime, $\epsilon = 0.00129$, $\eta = 0.01$, $k = 4.23$, We = 5000

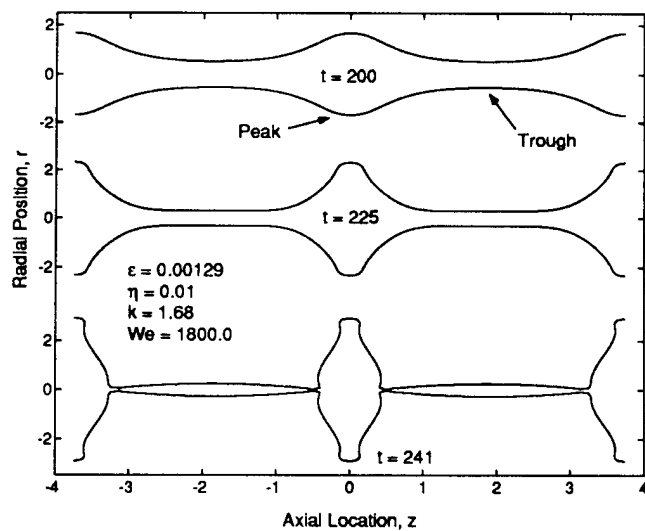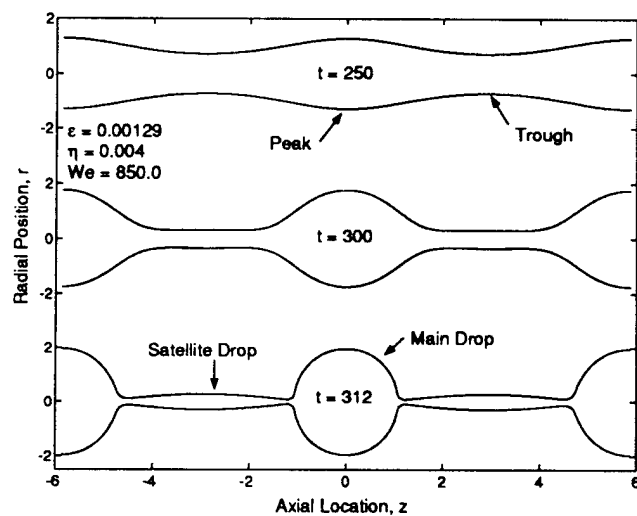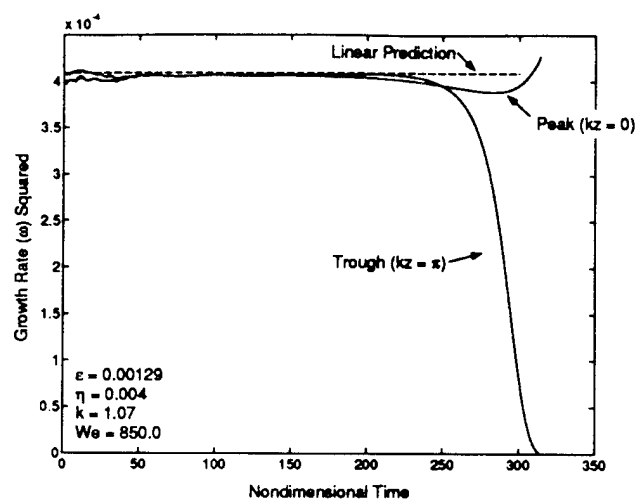FIG. 9. Comparison of the BEM to the Drop Sizes of Rutland and Jameson[8] (o) and Lafrance[7] (x) for Main and Satellite Drops, $\epsilon = 0.00129$
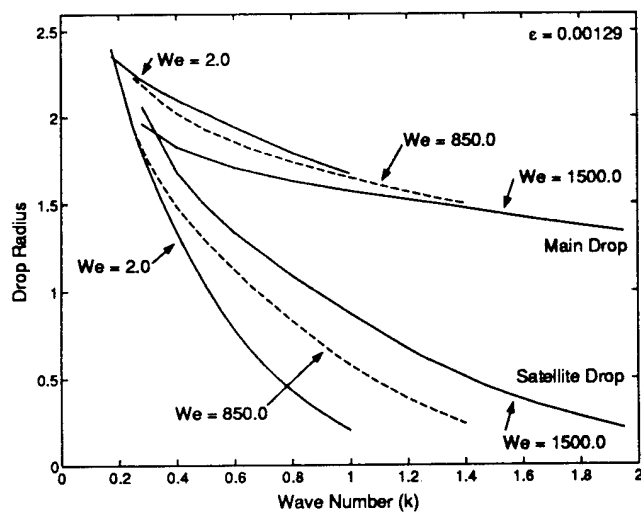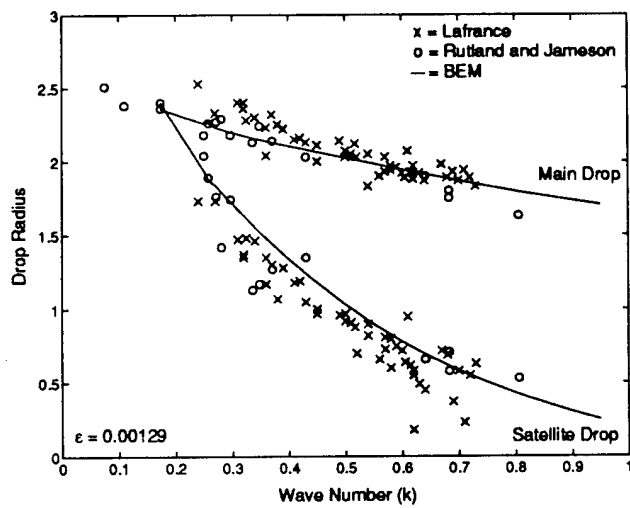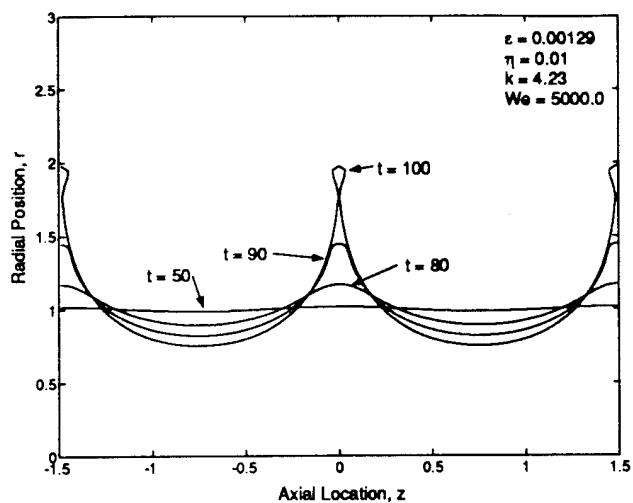
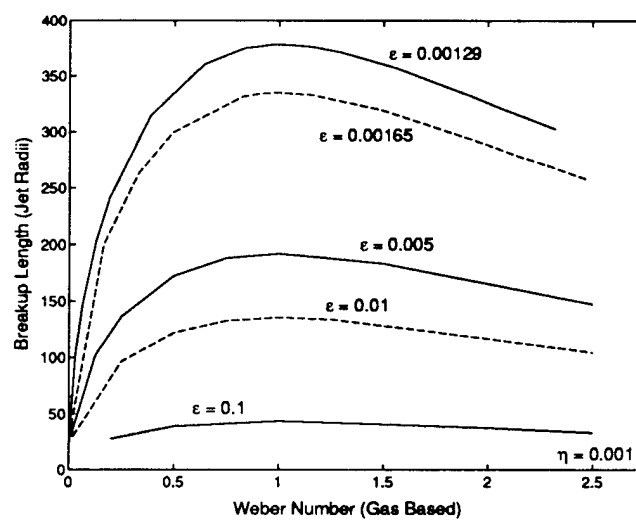FIG. 10. Drop Size versus Wave Number for $\epsilon = 0.00129$, We = 2, 850, 1500

FIG. 11. Breakup Length versus Gas Based Weber Number for $\epsilon = 0.00129$ (—), 0.00165 (– –), 0.005 (—), 0.01 (– –), 0.1 (—)

(a)

(b)

33

35
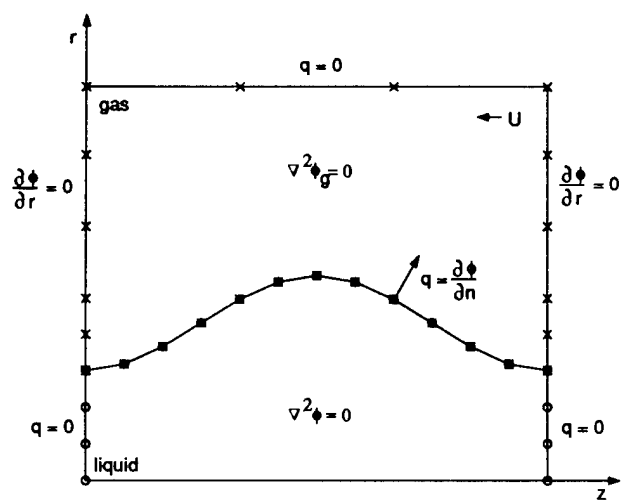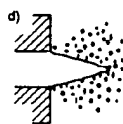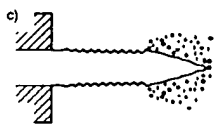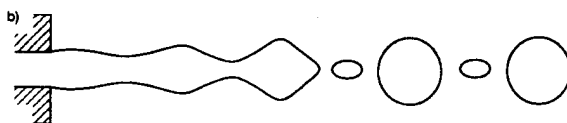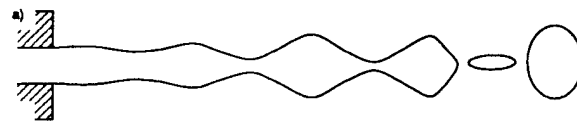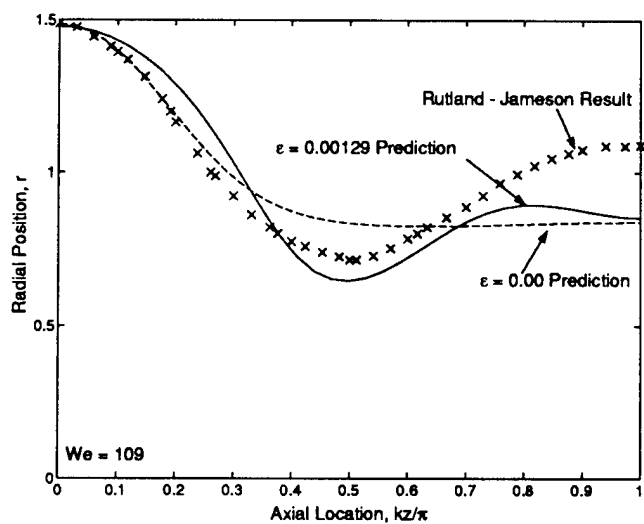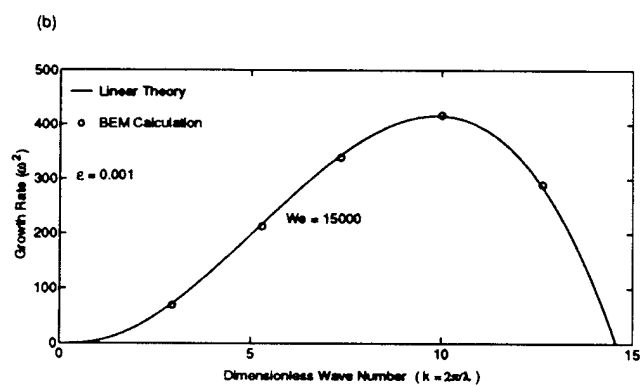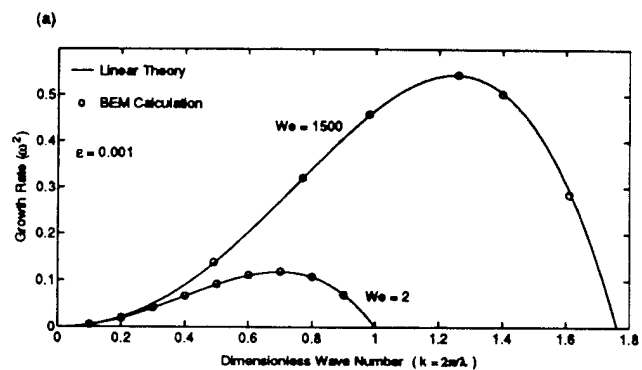
Appendix C

Manuscript Submitted to Atomization and Sprays

A BOUNDARY ELEMENT METHOD FOR ATOMIZATION OF A FINITE LIQUID JET

J. H. Hilbing*, S. D. Heister† and C. A. Spangler*

* Graduate Research Assistant

† Associate Professor, School of Aeronautics and Astronautics, Purdue University, W. Lafayette, IN

Abstract

A Boundary Element Method (BEM) has been developed to investigate the nonlinear evolution of the surface of liquid jets injected from circular orifices. The current treatment focuses on the low speed jet in which liquid viscosity and gas-phase pressure interactions are of minor importance. The model properly reflects both the presence of the orifice as well as the internal flow geometry. The model has been validated against nonlinear droplet oscillation calculations of other researchers. Results are presented for flows within the dripping and Rayleigh breakup regimes.

Introduction

The atomization of liquid jets is a fundamental problem of fluid mechanics. The behavior of this complex process is of engineering interest in numerous applications such as fuel injectors, paint applicators, and ink jet printers (to name just a few). For this reason, the atomization process has been studied by a large number of researchers, both experimentally and analytically.

For those seeking analytic solutions related to this problem, the nonlinearity associated with the free surface boundary condition represents a formidible obstacle. Many early works effectively eliminated this nonlinearity by implementing a linear stability analysis on an infinite cylindrical column of fluid in which free surface boundary conditions are employed on the undisturbed interface. A good summary of these works is provided in Reitz and Bracco [1] and Sterling and Sleicher [2]. More recently, Leib and Goldstein [3] effectively included the presence of the orifice in a linear analysis which also included the effect of injection velocity profile on jet stability. Computational models [4,5] have also made use of results from the linear

analyses, combined with one-dimensional mass and momentum balances to effectively model the atomization process.

The increased computational resources available during recent years has led analysts to the development of nonlinear models of these free surface flows. Traditional computational fluid dynamics (CFD) approaches are difficult to implement in these problems due to the large distortion of the grid which occurs near the droplet pinch-off event. Deng and Jeng [6] have had success in modeling a liquid droplet (in a gas flow) in this manner, but the solution accuracy is greatly diminished if the droplet surface is highly distorted.

Other researchers have employed the Volume of Fluid (VOF) technique pioneered by Hirt and Nichols [7]. This technique has the advantage of being able to treat a large number of droplets which are interpolated from a fixed (generally cartesian) grid. However, the free surface must be interpolated from existing nodal locations which leads to great difficulties in obtaining accurate representation of surface curvature. While this approach is useful for modeling a droplet field within a spray [8,9], early stages of the atomization process are more difficult to handle.

Recently, Boundary Element Methods (BEMs) have been utilized to accurately model free surface flows involving droplets [10] and liquid jets [11-13] for free surface flows. Since these techniques utilize a "grid" of nodes placed only on the boundary of the domain, they can handle large surface distortions and droplet pinchoff without complications. Previous liquid jet studies have revealed the presence of satellite droplets in the Rayleigh [11] and first wind-induced [12] regimes through the examination of a single wave in a liquid jet of infinite axial extent. However, these models have not investigated the effects of the presence of the orifice due to the infinite jet assumption. In very low speed (dripping) and high speed (atomization) flows, the orifice interaction can be important since breakup occurs in close proximity to the exit plane.

In this paper, we describe a BEM capable of addressing the finite-length liquid jet. The model is described in the following section. Following this description, we discuss validation of the code for a nonlinear droplet oscillation problem. Nonlinear results are discussed for dripping flows as well as flow within the Rayleigh regime. Finally, a model of a fountain is briefly described.

Model Development

We assume an axisymmetric, incompressible, inviscid flow in which gas pressure variations are negligible. The flow regime under which these assumptions are valid is one in which the liquid velocity is low since viscous forces will become important when the ratio $\mu v/\sigma$ approaches unity. Under these assumptions, the unsteady liquid flow is described by Laplace's equation:

$$\nabla^2 \phi = 0 \tag{1}$$

where ϕ is the velocity potential defined as the function whose gradient is simply the velocity, i.e. $\nabla \cdot \phi = \vec{v}$.

Following Liggett and Liu [14], the BEM formulation of Eq. (1) becomes:

$$\alpha \phi(\vec{r_i}) + \int_\Gamma [\phi \frac{\partial G}{\partial n} - qG] d\Gamma = 0 \tag{2}$$

where $\phi(\vec{r_i})$ is the value of the potential at a point $\vec{r_i}$, Γ denotes the boundary of the domain, and G is the Green's function corresponding to Laplace's equation. Since Eq. (2) involves an integration only around the boundary, we need not discretize the entire domain. It is presumed that either ϕ or $q = \partial\phi/\partial n$ is specified at each "node" on the boundary. Here n is the outward normal to the boundary so that q represents the velocity normal to the boundary. The quantity α in Eq. (2) results from singularities introduced as the integration passes over the boundary point, $\vec{r_i}$. For an axisymmetric formulation, α is equal to the angle between successive nodes on the boundary.

The geometry for the integration process is shown in Fig. ??. If we let r and z denote radial and axial coordinates, respectively, and denote the base point with subscript "i", the Green's function solution to the axisymmetric Laplacian can be written:

$$G = \frac{4rK(p)}{\sqrt{a}} \tag{3}$$

where

$$a = (r + r_i)^2 + (z - z_i)^2 \tag{4}$$

and

$$p = \frac{(r - r_i)^2 + (z - z_i)^2}{a} \tag{5}$$

and $K(p)$ is the complete elliptic integral of the first kind (for efficiency this quantity is calculated using a curve fit [15].

Physically, the Green's function represents the contribution of a source (at location $\vec{r}$) of strength 2π as sensed at the "base point", $\vec{r_i}$. While the quantity $\partial G/\partial n$ represents the contribution of a doublet as sensed at the base point. By properly weighting all these source and doublet strengths, we can solve Laplace's equation for arbitrary boundary conditions. Derivation of $\partial G/\partial n$ for this axisymmetric problem is quite involved. Gipson [16] gives:

$$\frac{\partial G}{\partial n} = \frac{-1}{2\sqrt{a}} \left[\hat{n}_r K(p) + \frac{E(p)}{(r-r_i)^2 + (z-z_i)^2} \left[\left((r-r_i)^2 - (z-z_i)^2 \right) \hat{n}_r + 2r\hat{n}_z(z-z_i) \right] \right] \tag{6}$$

with the quantities $\hat{n}_r$ and $\hat{n}_z$ being the components of the outward normal unit vector in the radial and axial directions, respectively, while $E(p)$ is the complete elliptic integral of the second kind.

Performing the desired integration around the boundary of the domain results in an algebraic system of equations. In order to perform this integration, it is necessary to assume a behavior for ϕ and q over the length of an element. We assume that both ϕ and q vary linearly over the length of an element. With this assumption, the values for the potential of the element bounded by nodes j and $j+1$ is:

$$\phi = \phi_j \frac{\Gamma_{j+1} - \Gamma}{\Gamma_{j+1} - \Gamma_j} + \phi_{j+1} \frac{\Gamma - \Gamma_j}{\Gamma_{j+1} - \Gamma_j} \tag{7}$$

with an analogous expression for the velocity, q. Using linear elements, Eq. (2) is divided into two separate integrals:

$$\int_\Gamma q G d\Gamma = \sum_{j=1}^{n-1} [q_j I_1(i,j) + q_{j+1} I_2(i,j)] \tag{8}$$

and

$$\int_\Gamma \phi \frac{\partial G}{\partial n} d\Gamma = \sum_{j=1}^{n-1} [\phi_j I_3(i,j) + \phi_{j+1} I_4(i,j)] \tag{9}$$

where

$$I_1 = \int_{\Gamma_j}^{\Gamma_{j+1}} \frac{\Gamma_{j+1} - \Gamma}{\Gamma_{j+1} - \Gamma_j} G d\Gamma \tag{10}$$

$$I_2 = \int_{\Gamma_j}^{\Gamma_{j+1}} \frac{\Gamma - \Gamma_j}{\Gamma_{j+1} - \Gamma_j} G d\Gamma \tag{11}$$

$$I_3 = \int_{\Gamma_j}^{\Gamma_{j+1}} \frac{\Gamma_{j+1} - \Gamma}{\Gamma_{j+1} - \Gamma_j} \frac{\partial G}{\partial n} d\Gamma \tag{12}$$

and

$$I_4 = \int_{\Gamma_j}^{\Gamma_{j+1}} \frac{\Gamma - \Gamma_j}{\Gamma_{j+1} - \Gamma_j} \frac{\partial G}{\partial n} d\Gamma \tag{13}$$

The integrals I_1 through I_4 are calculated using four point Gaussian Quadrature [15]. Using the integrals I_1 through I_4, we create D and S matrices which contain doublet and source contributions, respectively. From Eqs. (10) and (11), we can write:

$$S_{i,j} = I_{1_{i,j}} + I_{2_{i,j-1}} \qquad D_{i,j} = I_{3_{i,j}} + I_{4_{i,j-1}} \tag{14}$$

The integration of Eq. (2) results in a system of algebraic equations of the form:

$$[D]\{\phi\} = [S]\{q\} \tag{15}$$

with the values of α incorporated into diagonal elements of the D matrix. To solve this system of equations, all the unknown terms are "pivoted" by interchanging the columns of the appropriate matrices. With all the known values on the right hand side, the algebraic system of equations can be written in standard form:

$$[A]\{x\} = \{b\} \tag{16}$$

where x is the vector of unknown boundary values of ϕ or q. The resulting matrix A is fully populated. We solve this system of equations by a Crout Method LU decomposition taken from *Numerical Recipes in FORTRAN* [17].

This method requires $n^3/3$ operations to solve the system, while the popular Gaussian elimination method requires $2n^3/3$ operations. This reduction in the number of operations by a factor of two is a significant improvement in the computation time required for large systems of equations such as those solved here.

Centerline, Corner, and Self-Adjoint Nodes

The calculation of the integrals in Eqs. (10)-(13) is straightforward except for three special cases: nodes on the centerline of the domain, nodes on the corners of the domain, and self-adjoint nodes.

¿From the Green's function, Eq. (3), both G and $\partial G/\partial n$ vanish along the centerline ($r = 0$) of the domain. Therefore, no nodes need to be placed along the centerline of the domain except at the ends. At the endpoints, the values of G and $\partial G/\partial n$ are not zero since the integration at these points is not directly along the centerline. At the first node, the $I_1(1,1)$ and $I_2(1,1)$ terms are equal to πr_2, where r_2 is the radial distance to the second node. The $I_3(1,1)$ and $I_4(1,1)$ terms are zero. An examination of the last node in the domain yields an equivalent result.

At the corners of the domain, the unit normal and normal velocity are multivalued. In Fig. ??, for example, the node labeled k has both a horizontal and vertical velocity. The boundary element method only allows for the calculation of one velocity or potential at any one node. This characteristic of the BEM requires special treatment of corner nodes. At this corner node, k, the general S matrix calculation can be written:

$$
\begin{aligned}
Sq = \ldots \quad & + [I_1(i, k-1) + I_2(i, k-2)]q_{k-1} \\
& + [I_2(i, k-1)]q_k^- + [I_1(i, k)]q_k^+ \\
& + [I_1(i, k+1) + I_2(i, k)]q_{k+1} +
\end{aligned}
\tag{17}
$$

where $k-1$ and $k+1$ are the node before and the node after the corner, respectively. The elements of the S matrix are modified at the corners by using values of I_1 and I_2 consistent with the desired solution. For corners where the q_k^+ velocity is zero, such as an orifice exit or nozzle inflow, the element of the S matrix is equal to the appropriate value of I_2 only.

Self-adjoint nodes are defined as the nodes in the integration where $i = j$ and $i = j + 1$. In these two cases, the elliptic integral $K(p)$ is singular due to p having a value of zero at one end of the integration. To treat this singularity, the curve fit used for $K(p)$ from Abramowitz and Stegun [15] is divided into singular and nonsingular parts:

$$
K(p) = K(p)^* - b_0 \ln(p) = K(p)^* - \frac{1}{2} \ln \left[\frac{(r - r_i)^2 + (z - z_i)^2}{(r + r_i)^2 + (z - z_i)^2} \right]
\tag{18}
$$

where $K(p)^*$ represents the nonsingular part of the elliptic integral. Substituting into Eq. (10), the new expression can be divided into singular and nonsingular parts. The nonsingular parts are treated similarly to the nonsingular equation for I_1. For the singular parts, we make the substitution $\xi = (\Gamma - \Gamma_j)/\Delta\Gamma_j$, which results in a third equation that can also be divided into singular and nonsingular parts. The singular part of this new equation is computed with special Gaussian quadrature [15]. The final result at the point $i = j$ is:

$$
I_1(i, i) = \frac{\Delta\Gamma_j}{2} \int_{-1}^{1} \frac{1 - \xi}{2} (G)_s \, d\xi - \Delta\Gamma_j \int_0^1 (1 - \xi) \frac{4r}{\sqrt{a}} \ln \xi \, d\xi
\tag{19}
$$

where:

$$
(G)_s = \frac{4r}{\sqrt{a}} \left(K(p)^* + \ln \frac{\sqrt{a}}{\Delta\Gamma_j} \right)
\tag{20}
$$

43

The same approach is applied to the I_2 through I_4 terms, and yields:

$$I_2(i,i) = \frac{\Delta\Gamma_j}{2}\int_{-1}^1 \frac{1-\xi}{2}(G)_s\, d\xi - \Delta\Gamma_j \int_0^1 \frac{4r}{\sqrt{a}}\xi\ln\xi d\xi \tag{21}$$

$$I_3(i,i) = \frac{\Delta\Gamma_j}{2}\int_{-1}^1 \frac{1-\xi}{2}\left(\frac{\partial G}{\partial n}\right)_s d\xi + \Delta\Gamma_j \int_0^1 (1-\xi)\frac{2\hat{n}_r}{\sqrt{a}}\ln\xi d\xi \tag{22}$$

$$I_4(i,i) = \frac{\Delta\Gamma_j}{2}\int_{-1}^1 \frac{1-\xi}{2}\left(\frac{\partial G}{\partial n}\right)_s d\xi + \Delta\Gamma_j \int_0^1 \frac{2\hat{n}_r}{\sqrt{a}}\xi\ln\xi d\xi \tag{23}$$

where,

$$\left(\frac{\partial G}{\partial n}\right)_s = \frac{-2}{\sqrt{a}}E(p)\left[\frac{\left[(r-r_i)^2 - (z-z_i)^2\right]\hat{n}_r + 2\hat{n}_z r(z-z_i) + \hat{n}_r\left(K(p)^* + \ln\frac{\sqrt{a}}{\Delta\Gamma_j}\right)}{(r-r_i)^2 + (z-z_i)^2}\right] \tag{24}$$

The self-adjoint terms at $i = j + 1$ are examined with the same procedure, and results similar to Eqs. (19) and (21)-(23) are obtained.

Free Surface Module

For nodes lying outside the orifice, boundary conditions for the "Laplace Solver" discussed above are derived from an examination of the free surface boundary condition. This condition will enable us to determine the time-dependent variation of ϕ on the free surface. We employ a procedure similar to that of Longuet-Higgins and Cokelet [18] to effectively track the free surface. If we permit surface nodes to move at the instantaneous velocity, flow kinematics require:

$$\frac{Dz}{Dt} = \frac{\partial\phi}{\partial z} \qquad\qquad \frac{Dr}{Dt} = \frac{\partial\phi}{\partial r} \tag{25}$$

where the notation $D()/Dt$ implies a material or Lagrangian derivative. Recognizing that our BEM solver will return velocities normal to the surface, we employ the velocity transformations:

$$\frac{\partial\phi}{\partial r} = \frac{\partial\phi}{\partial s}sin(\beta) + qcos(\beta) \qquad\qquad \frac{\partial\phi}{\partial z} = \frac{\partial\phi}{\partial s}cos(\beta) - qsin(\beta) \tag{26}$$

where β is the local wave slope and $\partial\phi/\partial s$ is the velocity tangential to the local surface, as shown in Fig. ??. This tangential velocity is calculated using 5-point centered differences on ϕ, except for nodes adjacent to the orifice, where a 3-point formula is employed.

The local wave slope, β, is calculated following the formulation of Medina [19]. For each node, a parabola is defined such that it passes through the previous node, the node in question, and the following node. The slope of the surface is given by the tangent to the parabola at the central node.

44

We obtain a means of updating ϕ on the surface boundary by considering the unsteady Bernoulli relation. For our problem, after transforming the time derivative of ϕ from Eulerian to Lagrangian representation, the dimensionless representation of this equation is:

$$\frac{D\phi}{Dt} = \frac{1}{2}(\nabla\phi)^2 - \frac{\kappa}{We} + \frac{Bo}{We}z \tag{27}$$

where $We = (\rho v^2 a)/\sigma$ is the Weber number, $Bo = (\rho g a^2)/\sigma$ is the Bond number, and κ represents the local surface curvature. Here ρ is fluid density, a is the radius of the orifice, σ is the fluid surface tension, and g is the acceleration due to gravity.

The curvature of the surface is calculated using a parametric form from Smirnov [20].

$$\kappa = \frac{z'}{r\sqrt{(r')^2 + (z')^2}} + \frac{r'z'' - r''z'}{\left[(r')^2 + (z')^2\right]^{\frac{3}{2}}} \tag{28}$$

where the derivative terms are with respect to the distance along the surface. Note that $(r')^2 + (z')^2 = 1$ for derivatives with respect to the distance along the surface. We calculate these derivatives using five point centered difference approximations for nonuniform grid spacing.

Integration

In order to integrate Eqs. (25) and (27), we employ a fourth-order Runge-Kutta method [21]. The accuracy of this method requires four evaluations of the function for each step in time. Even with this large computational cost, the method has a significant benefit to the problem solved here. This benefit is in "self-starting". That is, the method does not require information from previous time steps. This self-starting ability allows for the addition or subtraction of nodes, the use of a variable time step, and for the regridding of the surface over time. Other popular fourth order methods, such as Adams-Bashforth-Moulton, are not self-starting and do not allow for these variations to occur.

Medina [19] recognized that the selection of a constant time step depends on the most demanding conditions during the surface evolution. He found the time when the droplets are about to be formed the most restrictive. We employ a method to dynamically modify the time step based on the surface velocities, so that the time step is decreased if the velocities become too large. In our method, no node is allowed to move more than a specified fraction of the grid spacing every time step. We calculate this local time step at every

node by dividing the maximum allowable distance by the velocity (the maximum of the axial and radial velocities) at that node. The time step used is the minimum of all calculated time steps and the initial time step set as an input to the program.

Numerical Smoothing

Several authors [10,18] have noted the appearance of "zig-zag" instabilities for BEM calculations running long periods of time. To avert this nonphysical kinking of the surface, we apply a smoothing function every time step which is an adaptation of the function used by Longuet-Higgins and Cokelet [18]:

$$\phi_j = (1 - C_s)\phi_j + \frac{C_s}{16}(-\phi_{j-2} + 4\phi_{j-1} + 10\phi_j + 4\phi_{j+1} - \phi_{j+2}) \tag{29}$$

where C_s is a smoothing constant between 0 and 1.

The value of C_s must be large enough the smooth out the point-to-point kinks in the surface, but should not add a significant amount of damping to the inviscid solution. Using the simulation of nonlinear droplet oscillations, various values of C_s were used to determine the appropriate magnitude of this constant. Values as large as 0.10 were found to decrease the total energy of the droplet. Therefore, we typically use a value near 0.01, which provided good results without damping the droplet energy.

Regridding

Since the surface nodes are allowed to move with the local surface velocity, the spacing between nodes changes in time. In order to keep the grid spacing roughly equal, the surface is remeshed every time step using cubic splines. Using the distance along the surface, s, as the spline parameter, the spline coefficients for $r(s)$, $z(s)$, and $\phi(s)$ are calculated by solving a tridiagonal system of equations for the first derivative coefficients [21]. The slope at the ends of the spline are calculated where appropriate using 5-point centered differences.

For the oscillating droplet case, the nodes are redistributed keeping the total number of nodes a constant. For the liquid jet, the grid spacing along the jet is held roughly constant, allowing the number of nodes to increase as the jet issues from the orifice, and decrease as droplets are shed from the calculation. As the liquid jet begins to neck down, a node is maintained at the point of minimum radius. For the jet results presented here, the grid spacing is kept near 20% of the orifice radius. A droplet is separated from the calculation

when the jet pinches below 5% of the orifice radius. Numerical experiments indicate that solutions are not sensitive to either of these tolerance values.

Model Validation - Nonlinear Droplet Oscillations

To validate the axisymmetric BEM solver and free surface modules, we use results for the oscillation of a liquid droplet in the absence of gravity. Lamb presents the linearized solution for small oscillations of a drop of liquid about the spherical form [22]. His results can be expressed (for a given mode, n):

$$r = a + \epsilon_n P_n(cos\theta)sin(\omega_n^0 t + \eta) \tag{30}$$

for the surface shape,

$$\phi = -\frac{\omega_n^0 a}{n} \left(\frac{r}{a}\right)^n \epsilon_n P_n(cos\theta)cos(\omega_n^0 t + \eta) \tag{31}$$

for the velocity potential inside the drop, and

$$(\omega_n^0)^2 = \frac{n(n-1)(n+2)\sigma}{\rho a^3} \tag{32}$$

for the frequencies. Here, σ is the surface tension, a is the unperturbed radius of the drop, and $P_n(cos\theta)$ is the Legendre polynomial of order n with θ the polar angle. Since the oscillating droplet does not have a characteristic velocity, we normalize velocities by the quantity $\sqrt{\sigma/(\rho a)}$. For the second mode, the non-dimensional frequency is given by $\omega_2^0 = \sqrt{8/We}$. Using 25 nodes on half a droplet with no smoothing or remeshing, a radius of 1 and a displacement of 0.05, the measured frequencies for the second mode from the BEM code for Weber numbers of 0.5 to 2.0 are within one tenth of one percent of the theoretical frequency.

Tsamopoulos and Brown [23] studied moderate oscillations of inviscid droplets by expanding to second order in amplitude. For the surface shape of the $n = 2$ mode, they found the result for $t = 0$:

$$r = a + \epsilon_2 P_2 + \frac{1}{2}\epsilon_2^2(-\frac{2}{5} + \frac{44}{462}P_2 + \frac{144}{175}P_4) \tag{33}$$

Figure ?? shows the initial shape for an amplitude of $\epsilon_2 = 0.40$ and the shape returned by the BEM calculation after half a period of oscillation.

Using 45 nodes along the half droplet, we calculated droplet oscillation frequencies for the $n = 2$ mode for initial disturbances of $\epsilon_2 = 0.05$ to 0.70. The results are presented in Fig. ?? as a percent frequency

47

shift from the linear result versus aspect ratio (length/width) at maximum prolate shape. Tsamopoulos and Brown considered moderate amplitude oscillations and only presented their own data to aspect ratios under 2. In this range, the BEM code returns frequency shifts within 0.5% of the analytic result. Extending the analytic result to aspect ratios up to about 3, we find frequency shifts within about 2% of the expected values. For these large disturbance oscillations, however, higher order corrections are needed if the droplet is to oscillate more than a few cycles.

Lundgren and Mansour [10] studied the oscillations of drops with weak viscous effects using the boundary integral method. They present results for various modes and initial conditions for inviscid droplet oscillations. We find excellent comparisons with our results for the same cases.

Dripping Flows

Figure ?? shows a typical computational domain for the finite-length liquid jet. In this figure, we consider a sharp-edge orifice of some given length and inside diameter. The model is capable of handling axisymmetric orifice geometries of arbitrary dimensions. We employ a "hybrid" set of boundary equations: nodes inside the orifice are fixed and have a specified normal velocity; nodes on the free surface move with the local velocity and have a known value of the velocity potential.

The initial shape of the jet is assumed to be cylindrical with a spherical endcap, moving with a uniform axial velocity. The initial length of the jet and the radius of the endcap are inputs to the initialization routine. By running the simulation through several pinches, subsequent results have been shown to be insensitive to this initial assumed geometry. Because of the assumed initial geometry, data for the first few droplet pinches is not included in the results. At low velocities, the breakup of a liquid jet occurs in the "dripping flow" regime. In this regime, the gas around the jet can be neglected, surface tension and gravity are the important parameters, and the droplet diameters are larger than the orifice diameter. Wu and Schelly [24] present experimental results on the effects of surface tension and temperature on the dynamics of a dripping faucet. Their nozzle geometry is shown in Fig. ??; the orifice is beveled 45 degrees, the inside length of the nozzle is 40 mm, and the inner and orifice radii are 5 mm and 1 mm, respectively. Using a continuously variable flow rate, they recorded a "dripping spectrum" (drop interval as a function of flow rate) for various

solutions of water and surfactant. Results indicate chaotic and bifurcated (bimodal) shedding frequencies over the range $0.625 < We < 1.05$ for the case where $Bo = 0.204$. For $We > 1.05$, the droplet interval increases with decreasing flow rate which implies an increasing jet length as We increases.

Figure ?? presents a typical time history for the droplet shedding process. As a droplet is shed, a disturbance is sent upstream. The interaction of this disturbance with the orifice has been found to be responsible for the chaotic/bifurcated behavior observed at low We values. It is interesting to note that a deterministic model can explain chaotic behavior of this type. Previous efforts [24] have focused on chaos theory to explain the observed behavior.

Figure ?? shows the droplet sizes as a function of the Weber number for conditions consistent with Wu and Schelly's experiment. We note the chaotic/bifurcation behavior over a range $0.6 < We < 1.4$ and drop sizes between 1.5 and 2.0 jet radii. Plotting a "dripping spectrum" with drop interval as a function of Weber number as shown in Fig. ??, we find that the chaotic region occurs at slightly higher Weber numbers and with shorter drop intervals than the results of Wu and Schelly. This difference is due to the stabilizing influence of viscosity in the actual measurements. However, the general character of the map is reproduced using the BEM calculation. The minimum drop interval tends to be 20 msec for all Weber numbers above about $We = 0.6$. The jet breakup length in this range of Weber numbers is shown in Fig. ??. As We (jet velocity) is increased, the jet breakup point reaches a location such that this disturbance has vanishing influence on the orifice and the chaotic/bifurcated behavior vanishes. Above Weber numbers of 1.9, the model predicts a dramatic increase in jet breakup length, signaling the start of the Rayleigh breakup regime.

Rayleigh Breakup

At moderate inflow velocities, the presence of the surrounding gas can still be neglected, and the jet breakup length increases as the inflow velocity is increased. Experimental measurements of flows consistent with the Rayleigh regime [25-28] show the presence of satellite drops formed during the nonlinear portion of the atomization process. These experiments were performed by using a forced oscillation frequency thus permitting investigation of the growth of instabilities over a range of wavelengths.

To simulate these experimental results, we employ a computational domain with fixed nodes only at the

orifice exit; the nozzle geometry is not modeled. We specify an inflow velocity along the entire orifice exit of the form:

$$q = \bar{q} \left[1 + \eta sin \left(kt \right) \right] \tag{34}$$

where $\bar{q}$ is the mean inflow velocity, η is the amplitude of the oscillatory disturbance, and k is the wave number of the perturbation. The calculation begins with a long column of fluid outside the orifice in order to insure that perturbations from the assumed spherical endcap do not influence the development of waves due to the imposed perturbation.

Simulations were run for $We = 100$ with $Bo = 0$ and 0.5292. The nonzero Bond number is consistent with water flow through a 2 mm radius orifice. The inflow velocity had a substantial perturbation of 3% of the mean velocity with a wave number of 0.7. We are forced to consider perturbations of this magnatude due to the large computational resources required for smaller amplitude simulations; i.e. small perturbations lead to very long jets. Since large jet lengths result in a large number of nodes along the surface and long computation times, we begin these simulations with a grid spacing of 50% of the orifice radius. After the jet has shed the initial fluid outside the orifice, the grid spacing was reduced to 20% of the orifice radius, and the simulations were continued through a number of droplet shedding events.

Figure ?? shows the jet profile for $Bo = 0$ at four equally spaced time intervals during the simulation. The first profile occurred at $t = 87.0$, and the region near the orifice is not shown in the figure. The numerical simulation shows the formation of the satellite droplets found in the experimental results. We calculate average main and satellite droplet radii of 1.793 and 0.986, respectively, and a breakup length of 38.8 orifice radii. For a wave number of $k = 0.683$ and $We = 112$, Rutland and Jameson [26] report droplet radii of 1.75 and 0.58. The difference between the BEM calculation and experimental result can be attributed to the amplitude of the perturbation. For example, Dressler [29] has shown that uniform-sized drops can be generated if the perturbation is of sufficient amplitude which implies that the satellite droplet grows in size with increasing perturbation magnatude.

When the effect of gravity is included in the simulation, the disturbance wavelengths were found to increase along the jet. A comparison of jet profiles for $Bo = 0$ and $Bo = 0.5292$ at $t = 71$ is shown in Figure ??. From the figure, it is obvious that some stretching is occurring for substantial perturbation modeled in this case. We have found that this phenomenon becomes increasingly important as the jet

50

perturbation velocity component is increased and is most pronounced near the orifice. We believe the stretching phenomena can be attributed to differences in surface tension in the axial and azimuthal directions. The azimuthal load carrying capability (roughly σ/a near the orifice) provides an effective buckling strength for the column of fluid as it is accelerated during the positive portion of the velocity oscillation. However, the axial contribution, which would provide tensile strength for the column during the negative portion of the velocity contribution is very small near the orifice since curvature in this plane is very nearly zero. For very small perturbations, this phenomena would not be evident since the jet would be under negliglible axial acceleration levels.

We have noted that this phenomena is present in the measurements of Rutland and Jameson [30] in which they measured the wave shape while driving a jet with a fixed frequency (and hence fixed wavelength) disturbance. A 5% increase in jet volume was noted for a case showing the wave profile just prior to breakup. While some of this discrepancy may be attributed to experimental error, the wave stretching phenomena described above could also explain this measured result.

Fountain Simulation

By specifying a negative Bond number, gravity can be directed opposite to the jet velocity vector, producing the simulation of a fountain. Figure ?? shows the jet profile at equal time intervals for a typical fountain simulation. In this case, we choose water flowing at 1 m/sec through a 1 cm radius orifice. The nozzle has length/diameter ratio of 0.5, and an inlet corner rounded at 20% of the orifice radius. Inflow is specified normal to a 3 cm radius hemisphere at a rate to give the desired outflow velocity. As the figure shows, the jet forms a mushroom-shaped cap of fluid which is terminated in a torus.

Conclusions

A numerical model using the boundary element method has been developed for the purpose of investigating the nonlinear evolution of low-speed the orifice presence for arbitrary internal geometry, and resolves the free surface of the jet with high resolves the free surface of the jet with high accuracy throughout the calculation. Multiple droplets can be removed from the simulation as they are pinched off from the liquid

jet, and both steady and unsteady injection processes can be handled. The mod. For dripping flows, chaotic and bifurcated droplet shedding is predicted using this deterministic model. For dripping flows, chaotic and bifurcated droplet shedding is predicted. We find that this behavior is explained by interactions of surface waves (generated during pinchoff) with the orifice. Results indicate that an abrupt transition from dripping flow to Rayleigh flow occurs at $We = 1.9$. The model predicts formation of iain and satellite droplets in the Rayleigh regime for oscillating inflow velocities. The acceleration due to gravity tends to stretch the disturbance wavelengths as the axial position of the wave increases.

Nomenclature

a = orifice radius

C_s = smoothing constant

D = doublet contribution matrix

$E(p)$ = complete elliptic integral of the second kind

G = free space Greens function

$I_1 - I_4$ = components of the D and S matrices

$K(p)$ = complete elliptic integral of the first kind

$\hat{n}_r$ = unit normal in radial direction

$\hat{n}_z$ = unit normal in axial direction

P_n = Legendre polynomial of order n

q = surface velocity in the normal direction

r = radial coordinate

S = source contribution matrix

t = time

z = axial coordinate

Bo = Bond number, $Bo = \rho g a^2 / \sigma$

We = Weber number, $We = \rho U^2 a/\sigma$

α = boundary point singularity contribution

β = surface slope

Γ = domain boundary

κ = surface curvature

ρ = density

σ = surface tension

ϕ = velocity potential

References

1. Reitz, R. D., and Bracco, F. V., "Mechanism of Atomization of a Liquid Jet", *Physics of Fluids*, **25**, pp. 1730-1742, October 1982.

2. Sterling, A. M., and Sleicher, C. A., "The Instability of Capillary Jets", *Journal of Fluid Mechanics*, **68**, 1975, pp. 477-495.

3. Leib, S. J., and Goldstein, M. E., "The Generation of Capillary Instabilities on a Liquid Jet", *Journal of Fluid Mechanics*, **168**, pp. 479-500, 1986.

4. Przekwas, A. M., Lee, J.-G., Gross, K. W., Chigier, N. A., and Eroglu, H., "Analytical and Experimental Study of Primary Atomization of Water Jets", Fifth International Conference on Liquid Atomization and Spray Systems, Gaithersburg, MD, pp. 831-832, 1991.

5. Sellens, R. W., "A Numerical Model of the Capillary Instability", ILASS-91, July 1991.

6. Deng, Z.-T., and Jeng, S.-M., "Numerical Simulation of Droplet Deformation in Convective Flows", AIAA-90-2309, AIAA/SAE/ASME/ASEE 26th Joint Propulsion Conference, 1990.

7. Hirt, L. W., and Nichols, B. D., "Volume of Fluid (VOF) Method for the Dynamics of Free Boundaries", *Journal of Computational Physics*, **30**, pp. 201, 1981.

8. Amsden, A. A., O'Rourke, P. J., and Butler, T. D., "KIVA-II – A Computer Program for Chemically Reactive Flows with Sprays", Los Alamos National Labs., LA-11560-MS, 1989.

9. Liang, P. Y., Fisher, S., and Chang, Y. M., "Comprehensive Modeling of a Liquid Rocket Combustion Chamber", *Journal of Propulsion and Power*, **2**, N. 2, pp. 97, March-April 1986.

10. Lundgren, T. S., and Mansour, N. N., "Oscillations of Drops in Zero Gravity with Weak Viscous Effects", *Journal of Fluid Mechanics*, **194**, pp. 479-510, 1988.

11. Mansour, N. N., and Lundgren, T. S., "Satellite Formation in Capillary Jet Break-Up", *Physics of Fluids A*, **2**, pp. 1141-1144, July 1990.

12. Spangler, C. A., and Heister, S. D., "Nonlinear Modeling of Jet Atomization in the Wind-Induced Regime", ILASS-94 Proceedings, 1994.

13. Tjahjadi, M., Stone, H. A., and Ottino, J. M., "Satellite and Subsatellite Formation in Capillary Breakup", *Journal of Fluid Mechanics*, **243**, 1992, pp. 297-317.

14. Liggett, J. A., and P. L.-F. Liu, *The Boundary Integral Equation Method for Porous Media Flow*, Allen and Unwin, London, 1983.

15. Abramowitz, M., and Stegun, F. A., eds., *Handbook of Mathematical Functions*, Dover Publications, 9th Ed., 1970.

16. Gipson, G. S., Boundary Elements Fundamentals, Topics in Engineering Volume 2 (C. A. Brebbia and J. J. Conner (ed.)), Computational Mechanics Publications, 1987.

17. Press, W. H., Teukolsky, S. A., Vetterling, W. T., and Flannery, B. P., *Numerical Recipes in FORTRAN, The Art of Scientific Computing*, Cambridge University Press, 2nd Ed., New York, 1992.

18. Longuet-Higgins, M. S., and Cokelet, E. D., "The deformation of steep surface waves on water. I. A numerical method of computation", *Proc. R. Soc. Lond. A*, **350**, pp. 1-26, 1976.

19. Medina, D. E., "On Droplets and Boundary Elements", Cornell University, FDA-89-12, 1989.

20. Smirnov, V. I., *A Course of Higher Mathematics, Volume II*, Pergamon Press, New York, 1964.

21. Kreyszig, E., *Advanced Engineering Mathematics*, John Wiley and Sons, New York, 6th Ed., 1988.

22. Lamb, H., *Hydrodynamics, 6th Ed.*, Dover Publications, 1982.

23. Tsamopoulos, J. A., and Brown, R. A., "Nonlinear Oscillations of Inviscid Drops and Bubbles", *Journal of Fluid Mechanics*, **127**, pp. 519-537, 1983.

24. Wu, X., and Schelly, Z. A., "The Effects of Surface Tension and Temperature on the Nonlinear Dynamics of the Dripping Faucet", *Physica D*, **40**, pp. 433-443, 1989.

25. Lafrance, P., "Nonlinear Breakup of a Laminar Liquid Jet", *Physics of Fluids*, **18**, pp. 428-432, 1975.

26. Rutland, D. F., and Jameson, G. J., "Theoretical Prediction of the Sizes of Drops Formed in the Breakup of Capillary Jets", *Chemical Engineering Science*, **25**, pp. 1689-1698, 1970.

27. Fenn III, R. W., and Middleman, S., "Newtonian Jet Stability: The Role of Air Resistance", *AIChE Journal*, **15**, pp. 379-382, 1969.

28. Goedde, E. F, and Yuen, M. C., "Experiments on Liquid Jet Instability", *Journal of Fluid Mechanics*, **40**, pp. 495-511, 1970.

29. Dressler, J. L., "Atomization of Liquid Cylinders, Cones, and Sheets by Acoustically Driven, Amplitude-Dependent Instabilities", International Conference for Liquid Atomization and Spray Systems (ICLASS-91), Paper No. 41, 1991.

30. Rutland, D. F. and Jameson, G. J., "A non-linear effect in the capillary instability of liquid jets," J. Fluid Mech. **46**, 267 (1971).
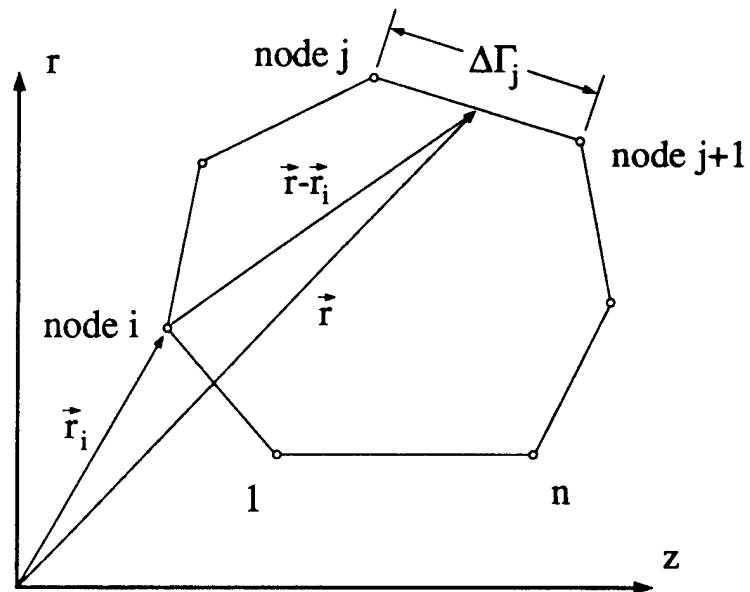
Figure 1: Geometry and Nomenclature for the BEM Formulation.
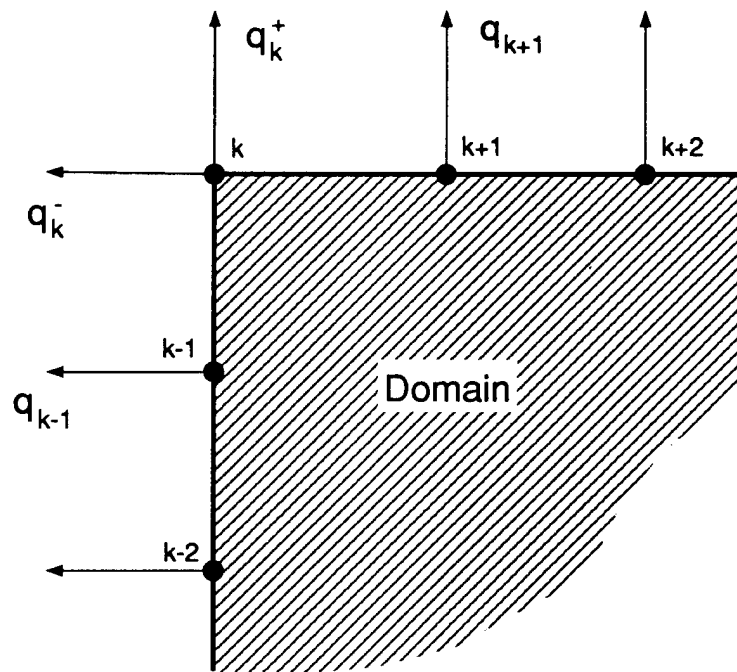
Figure 2: Corner Node with Two Unique Velocities.

57
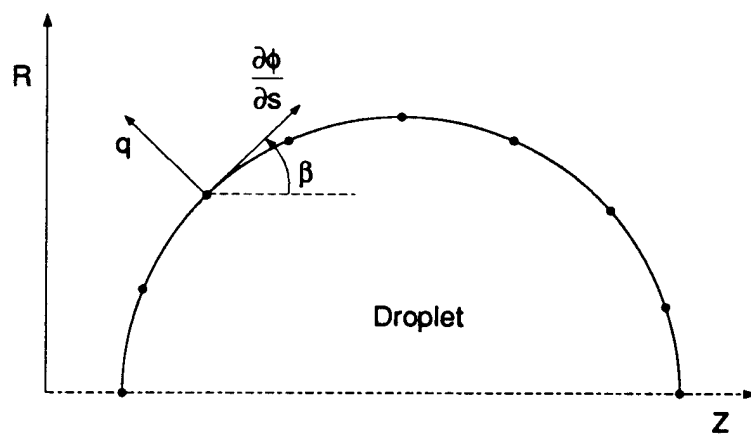
Figure 3: Surface Slope Definition.
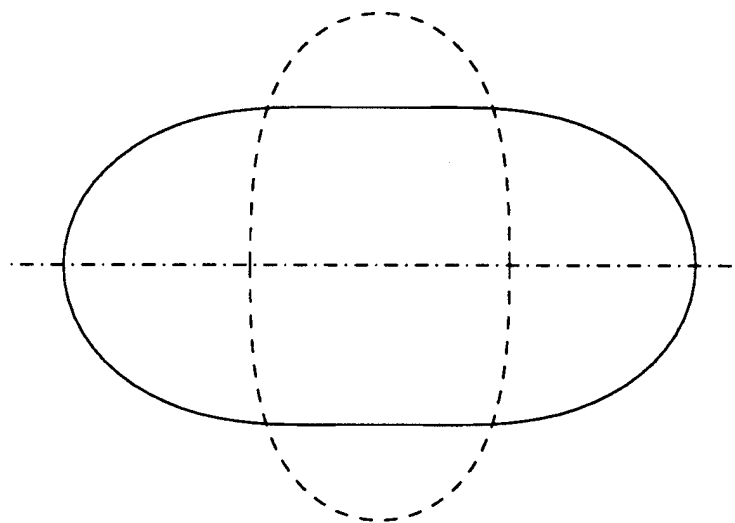
Figure 4: Droplet Shape for Mode $n = 2$ and $\epsilon_2 = 0.40$; — Initial Droplet Shape; – – Shape at $t = \tau/2$.

58
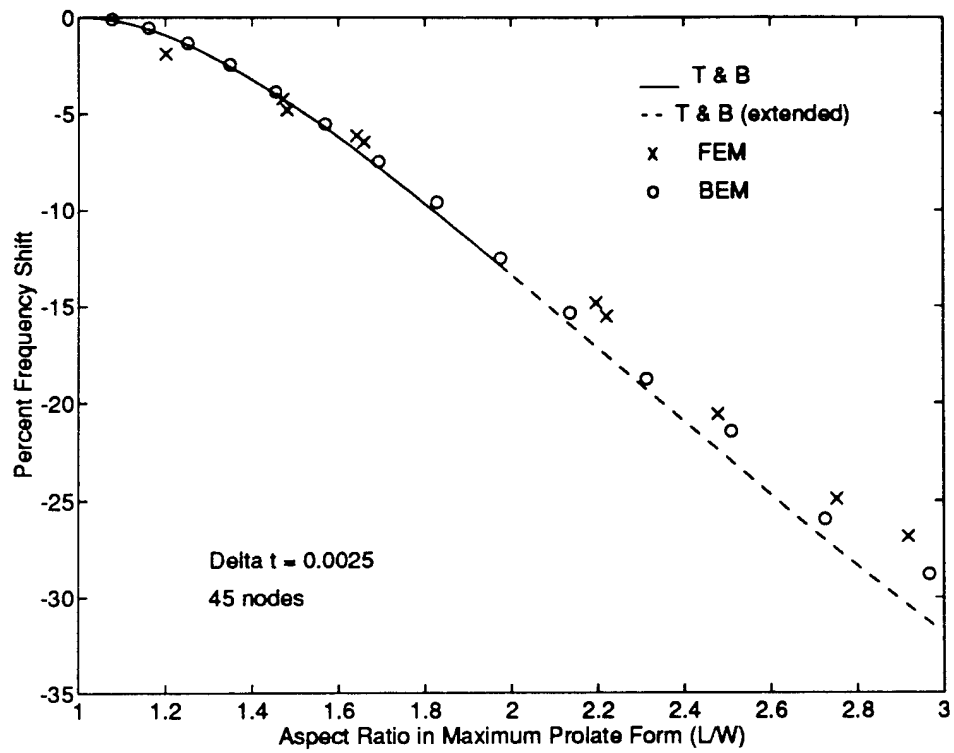
Figure 5: Frequency Shift for Mode $n = 2$ as a Function of Aspect Ratio.
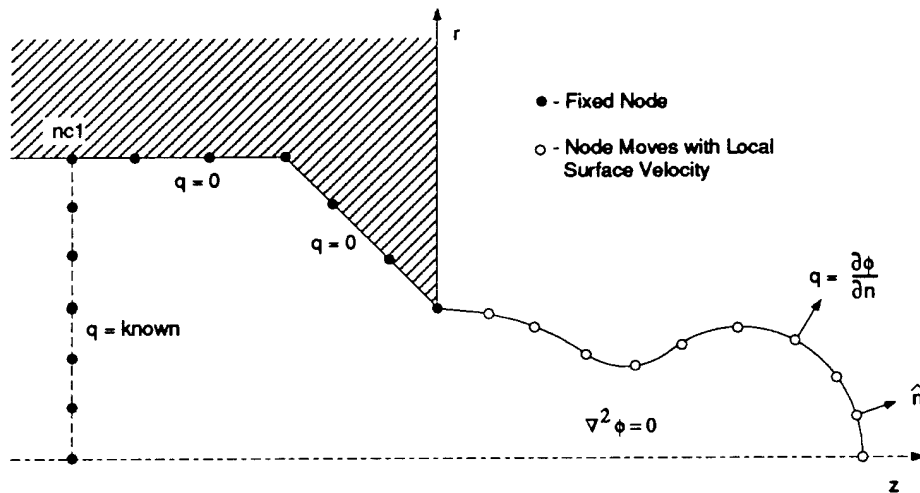
Figure 6: Finite-Length Liquid Jet Computational Domain.
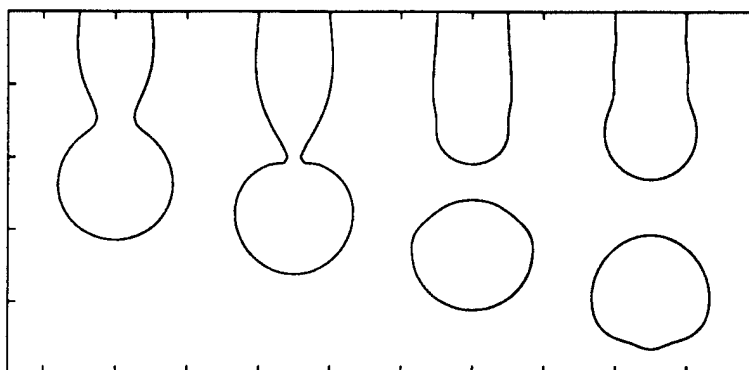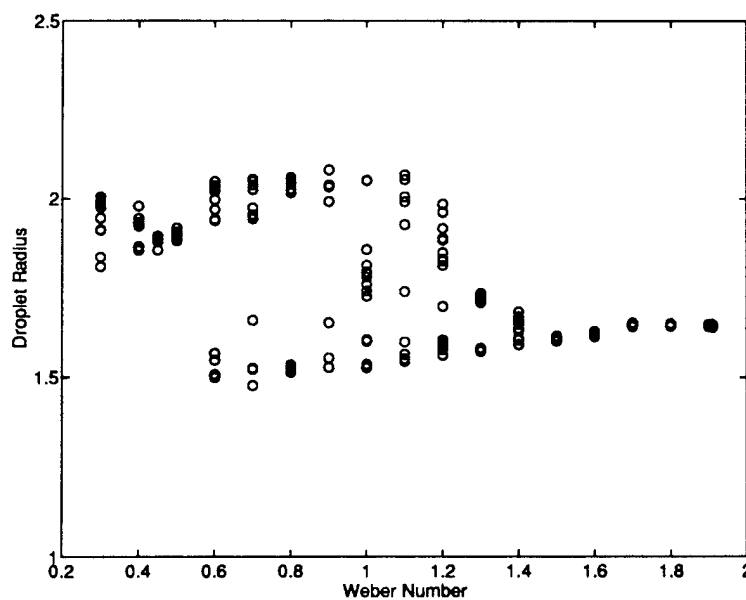
Figure 7: Typical Droplet Shedding History, We=1.45, Bo=0.204 (equal time intervals).

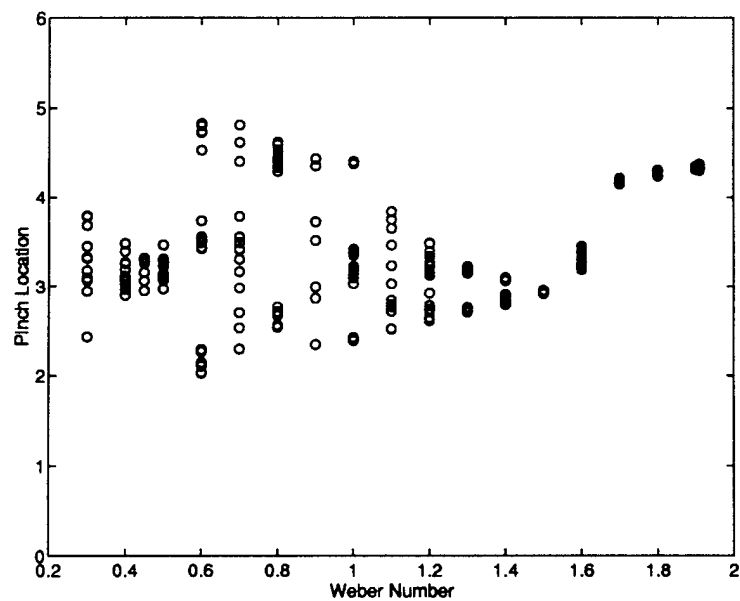Figure 8: Droplet Size for Dripping Flow, Bo=0.204.
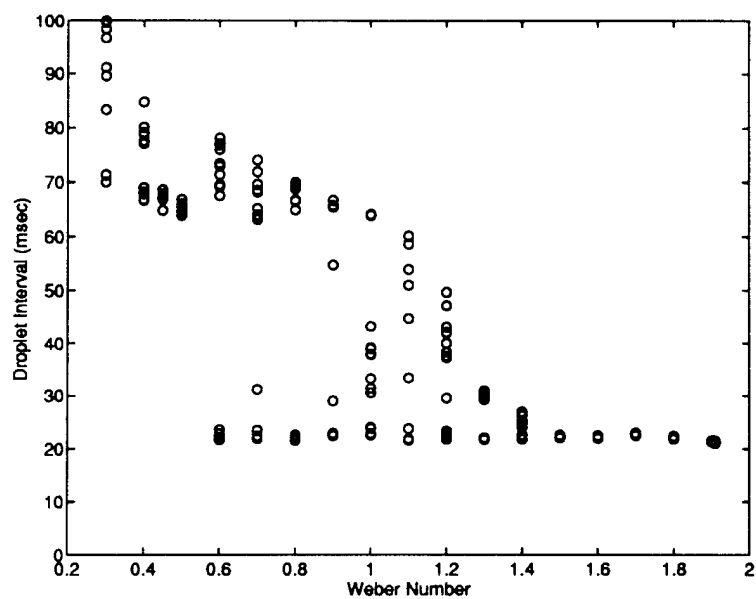
Figure 9: Dripping Spectrum for Bo=0.204.
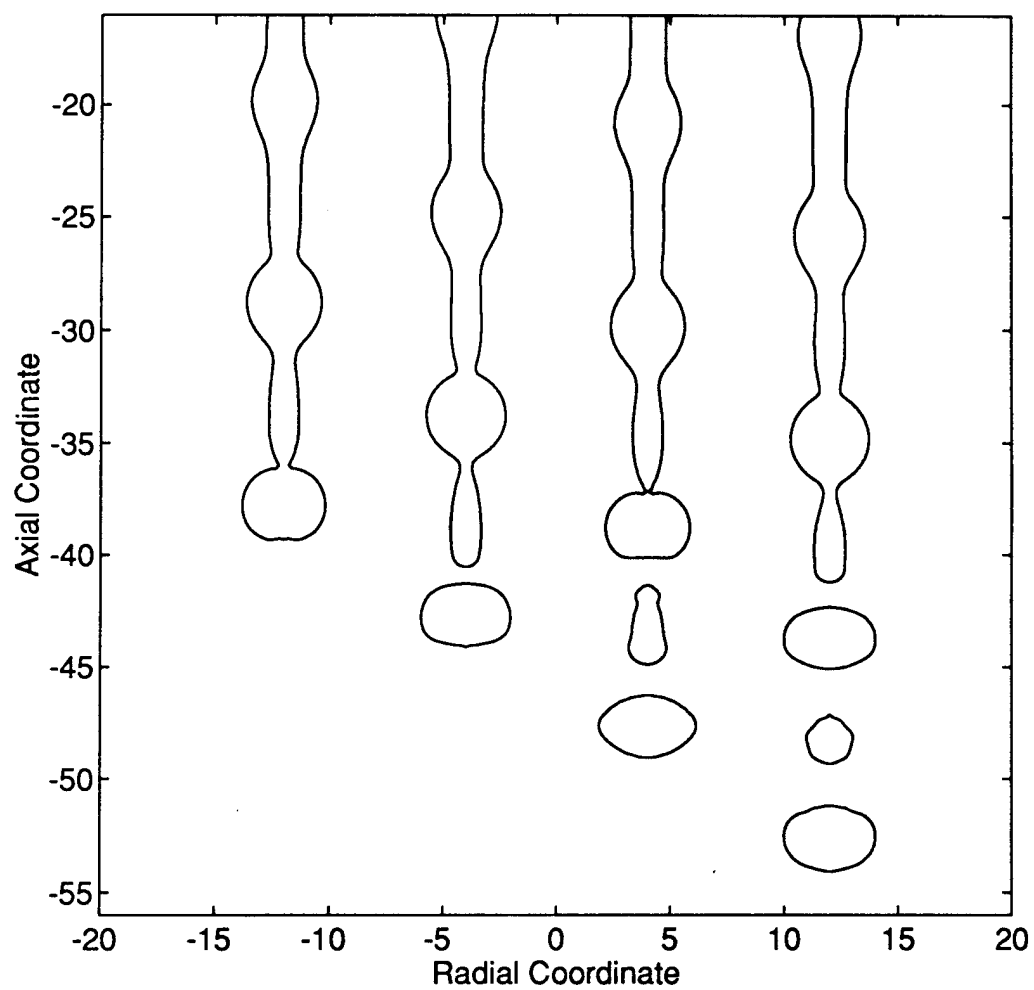

Figure 10: Breakup Length for Dripping Flow, Bo=0.204.

61

Figure 11: Jet Profile Near Pinch Location Showing Presence of Main and Satellite Droplets, We = 100, Bo = 0, and 3% Inflow Velocity Perturbation. Equal Time Intervals (dt=5.0), with the First Profile at $t = 87.00$.
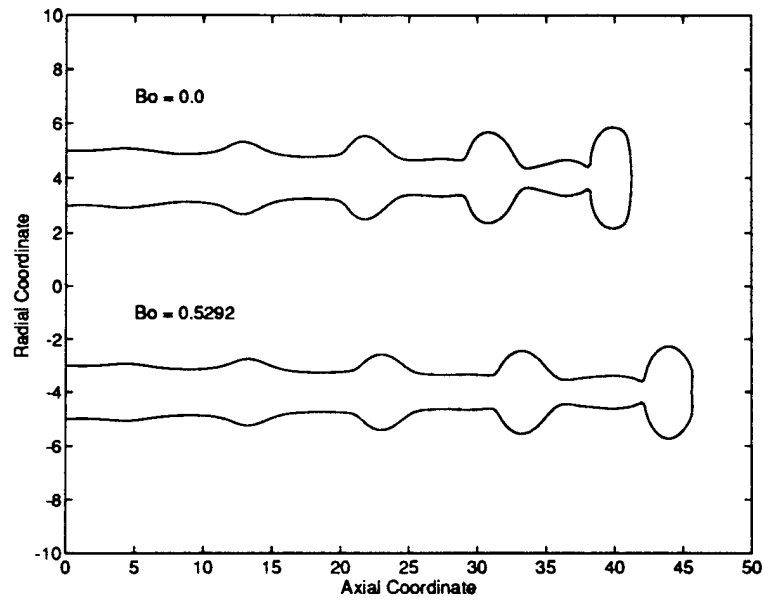
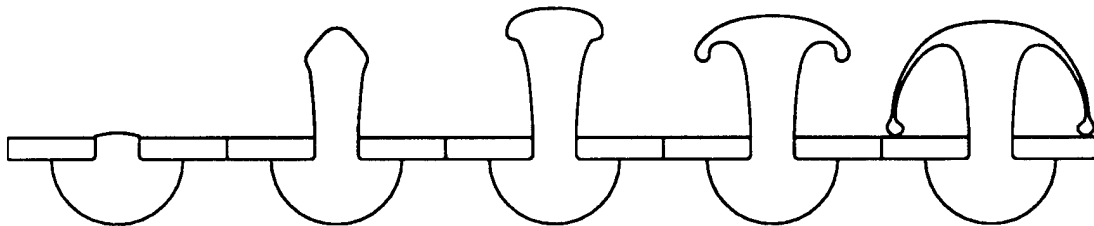Figure 12: Jet Profile Comparison for $We = 100$, $t = 71.00$, and 3% Inflow Velocity Perturbation.

Figure 13: Fountain Simulation. Equal Time Intervals.

63